Journal of Science and Technology in The Tropics

CONTENTS

SCAPS Simulation on P3HT: Graphene Nanocomposites Based Bulk-Heterojunction Organic Solar Cells

Nur Shakina Mohd Shariff , Siti Farhaniza Abd Samat, Puteri Sarah Mohamad Saad, and Mohamad Rusop Mahmood

NANO-Electronic Centre, Faculty of Electrical Engineering, Universiti Teknologi MARA, Shah Alam, 40450, Malaysia
(*corresponding author: kina_jb@yahoo.com)

Abstract   There has been an increasing interest towards organic solar cells after the discovery of conjugated polymer and bulk-heterojunction concept. Even though organic solar cells are less expensive than inorganic solar cells but the power conversion energy is still considered low. The main objective of this research is to investigate the effect of the P3HT's thickness and concentration towards the efficiency of the P3HT: Graphene solar cells. A simulation software that is specialized for photovoltaic called SCAPS is used in this research to simulate the effect on the solar cells. The solar cell's structure will be drawn inside the simulation and the parameters for each layers is inserted. The result such as the open circuit voltage (Voc), short circuit current density (Jsc), fill factor (FF), efficiency (η), capacitance-voltage (C-V) and capacitance-frequency (C-f) characteristic will be calculated by the software and all the results will be put into one graph.

Keywords   Organic Solar Cells, P3HT, Graphene, SCAPS

INTRODUCTION

Since the discovery of conjugated polymers [1-3] and bulk-heterojunction [4], organic solar cells has become a major field of studies in photovoltaic. Organic solar cells are well known nowadays due to its favourable properties such as easy fabrication, less expensive and lighter than inorganic based solar cells [5]. Most studied polymer till today is Poly(3-hexylthiophene) (P3HT), which possess excellent properties such as high electrical conductivity, high solubility in various solvent and also can be deposit over a large area, under low deposition temperature by using low-cost deposition technique [5-10]. P3HT is also said to possesses a high electrical mobility (µhole = 0.2 cm2/Vs) but it is still low compared to the electrical mobility of inorganic solar cells [5, 11]. Since P3HT is a donor material and a p-type semiconductor, it possesses higher whole mobility than electron mobility.

Recent photovoltaic studies shows new materials comprised organic-inorganic combination such as P3HT with carbon polymorph composites like CNTs and Graphene is developed in order to achieve a higher efficiency [5]. Since the discovery of Graphene in 2004, many studies on Graphene's properties has been done and it has been proven that Graphene has an excellent electrical characteristic such as an electron mobility of 10000 cm2/Vs and has a higher mobility and conductivity than carbon nanotubes (CNTs) [5, 12]. It is also reported that Graphene is a superb electron acceptor [5]. In this research, P3HT will be mixed with Graphene and will be used as a nanocomposite inside the solar cell. The existence of Graphene in P3HT also affects the capacitance of the thin film. To analyse the

charge transport in organic photovoltaic devices, capacitance (C) is being used. The capacitance-voltage characteristics can give a better insight into these devices when combined with current density-voltage (J-V) data [13]. C-V measurements can also provide wealth info of the device characteristic and can determine the semiconductor's parameters. Recent research has showed that the built- in voltage (Vbi) of the device can be obtained at the peak in the C-V characteristic [14]. In C-V characteristic, it is usually observe that only one peak is visible when the polarity is changed from reverse to forward when the bias is applied through the organic semiconductor [15-17].

The main problem for organic solar cells is the low power conversion efficiency because of low photocurrent. Low photocurrent in P3HT is due to low electron mobility (μelectron = 10-14 – 10-14 cm2/Vs) [5, 11]. In order to increase the electron mobility, P3HT will be mixed with a high electron mobility material such as Graphene. It also has been stated that low photocurrent is due to low absorption of incident light power [11, 18]. These two problems are mainly affected by the thickness of the active layer inside the solar cell. Therefore the objective of this research is the P3HT: Graphene layer will be simulated and a study on the effect of thickness and concentration towards the solar cell's characteristic will be measured.

METHODOLOGY

The structure of the solar cell is drawn in the software as shown in Figure 1. The parameters such as the bandgap, electron affinity and the concentration are fixed for each layer of the solar cell. The P3HT's thickness will be measured from 60nm to 100nm and for each thickness of P3HT, the concentration will be measured from 1x1013 till 1x1016 cm-3. Effect of the concentration will also be measured since carrier concentration is linked with electrical mobility. The open circuit voltage (Voc), short circuit current density (Jsc), fill factor (FF), efficiency (η), quantum efficiency (QE), the capacitance-voltage (C-V) and the capacitance-frequency will be calculated by the software.
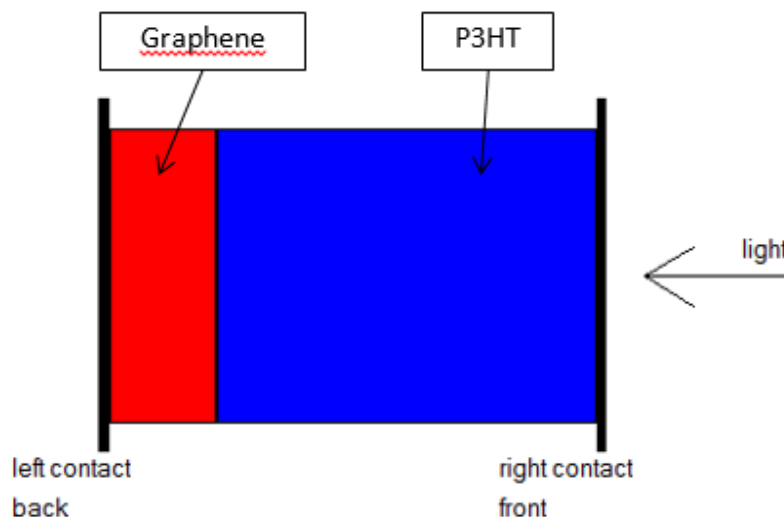
**Figure 1.** Solar cell structure of P3HT/Graphene layer

RESULTS AND DISCUSSION

According to the simulation result that is shown in Figure 2 (a), the current density shows the gap between the dark current and under illumination increases when the thickness of the active layer increases. For every thickness, the concentration range is from 1x1013 till 1x1016 cm-3. The layer that has a concentration of 1x1016 cm-3 have a better power conversion efficiency than the one with the concentration of 1x1013 cm-3. In order to generate more power, the gap between the dark current and under illumination should be bigger. Due to a bigger charge generation, the photocurrent will increase as the thickness of the P3HT: Graphene increases [11].

(a)   (b)
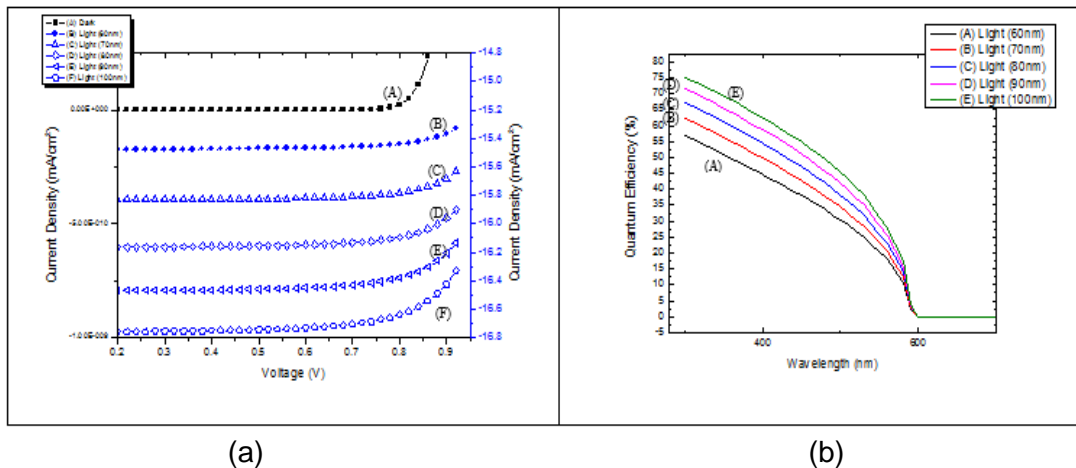
Figure 2. (a) Current density (Jsc) for every thickness at dark current and under illumination, (b) the quantum efficiency (QE) at different thickness of the active layer

From the quantum efficiency in Figure 2(b), it shows that the thicker the active layer, the higher the quantum efficiency. The quantum efficiency (QE) is only affected by the amount of the absorption light. When the active layer is thicker, more light will be absorbed to generate more photocurrent. The QE drop till 0 at around wavelength of 580nm because there are no more light absorbed at higher wavelength.

(a)   (b)
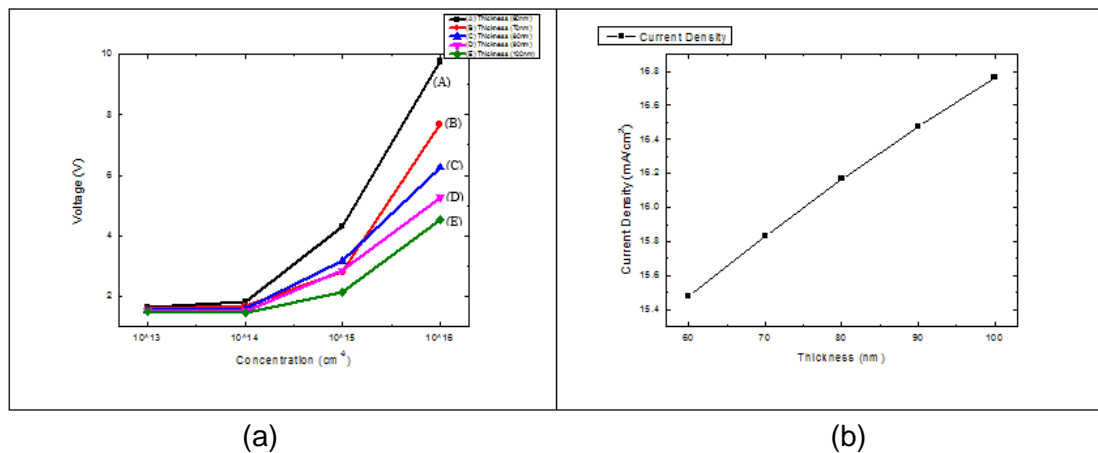
Figure 3. (a) The open circuit voltage (Voc) for every thickness and concentration, (b) The short circuit current density (Jsc) for every thickness

Figure 3(a) shows the effect of the layer's concentration towards the open circuit voltage (V_{oc}). V_{oc} increases as the concentration of the active layer increases and from the graph in Figure 3(a), the thickness of 60nm has the highest V_{oc} value at a concentration of 1×10^{16} cm^{-3} while the thickness of 100nm has the lowest V_{oc} value. The results from this graph shows that the thicker the active layer, the lower the voltage. Voltage is usually affected by the resistance. This proves that the thicker active layer has a lower voltage due to a higher series resistance [11].

Figure 3(b) shows the effect of the thickness towards the short circuit current density (J_{sc}) and from the results, the highest current density value is the layer with a thickness of 100nm whle 60nm has the lowest value. At a thickness of 100nm, the active layer has more area to generate current than the active layer that is only 60nm thick. It also have more carrier concentration, therefore the current is higher when the active layer is thicker. As stated from previous studies, when the thickness increases, the number of charges also increase due to more absorption [11].

(a)   (b)
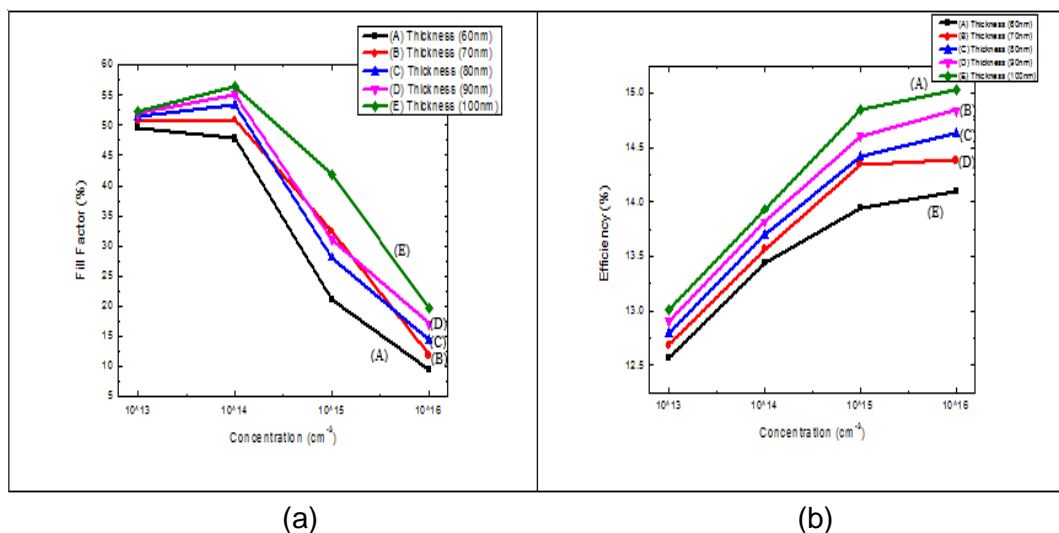
Figure 4. (a) Fill Factor (FF) for every thickness and concentration of P3HT, (b) the efficiency (η) for every thickness and concentration.

Figure 4(a) shows the fill factor results for each concentration. As shown, the fill factor decreases rapidly as the concentration rises. The fill factor then decreases as the thickness and concentration of the active layer increases from 1×10^{14} cm^{-3} to 1×10^{16} cm^{-3}. Fill factor can be defined as the ratio of the maximum power from the solar cell to the product of V_{oc} and I_{sc}. The *FF* decreases when the charge mobility is raised in polymer solar cells [11]. When the charge mobility increases, more charges can move through faster and will result in a higher photocurrent.

As in Figure 4(b), the efficiency rises when the concentration increases and the highest achieved efficiency is 15% at a thickness of 100 nm. A higher efficiency leads to a better device performance because more sunlight can be converted into electricity. Figure 4(b) shows that the thicker the active layer, the higher the power conversion efficiency. The efficiency is the most important result because it shows the performance of a solar cell. A higher efficiency leads to a higher performance solar cell. Efficiency is mainly affected by J_{sc}. As from Figure 3(b), the J_{sc} increase when the active layer gets thicker, due to that the efficiency also increased [11].

The effect of the P3HT's concentration towards the device's capacitance is shown in Figure 5 (a). Here, the thickness of the active layer is fixed at 100nm and the concentration is evaluated from 1.0 x 10^{13} cm^{-3} to 1.0 x 10^{16} cm^{-3}. From Figure 5 (a), only (D) shows drastic increases at 0.7 V while (A), (B) and (C) slowly decrease as the voltage increases. (D) also shows there is a built-in voltage inside solar cells. The capacitance increases in the forward direction and reach a peak at 0.86V. It has been reported that the peak came from mobile holes in donor materials [15]. This might occur due to the concentration of P3HT which increased from 1.0 x 10^{13} cm^{-3} to 1.0 x 10^{16} cm^{-3}. P3HT is p-type semiconductor, therefore it is more rich in hole concentration. When the hole concentration increases, the capacitance value will also increase. A closer look at the capacitance when the carrier concentration of 1.0 x 10^{16} cm^{-3}, it can be seen that the capacitance decreases at first until it reaches a voltage of 0.58V. Starting form 0.58V the capacitance increases rapidly till reach its peak at around 0.86V. The capacitance then decreases till 0.94V due to the limitation of the minority carriers concentration in the neutral regions of the device [14].
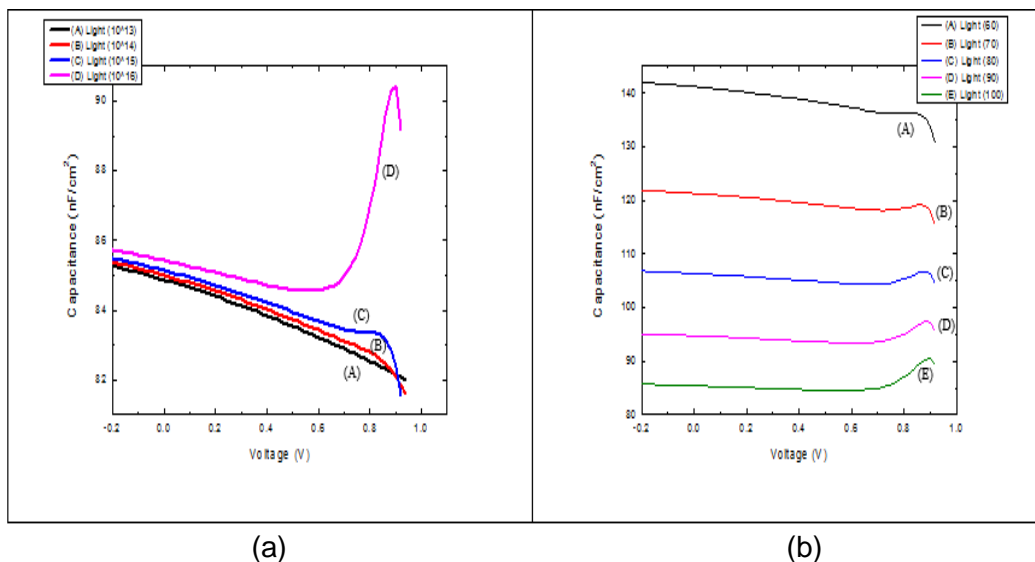
Figure 5. (a) C-V characteristic for every concentration, (b) C-V characteristic for different layer's thickness

Figure 5 (b) shows the effect of thickness towards the device's capacitance voltage. The voltage is fixed from -0.8V to 1.0V and the concentration is fixed at 1.0 x 1016 cm^{-3}. The thickness of P3HT is measured from 60 nm till 100 nm. As seen from Figure 5 (b), capacitance is high when the thickness of the active layer is at 60 nm and the capacitance is at its lowest when the thickness is 100 nm. Therefore, the capacitance increases as the thickness decreases. There is a slight rise at 0.84V for very thickness but as the thickness decrease, the peak also decreases. As explained above, the peak decreases due to the limitation of minority carriers concentration [14] in P3HT which is the hole concentration. When the thickness of the P3HT layer decreases, the hole concentration also decreases. This will lead to decrease in the peak. The peak for all thickness is also the same since it has been reported that the peak voltage is related to the bias voltage Vb_i [13]. The capacitance is inversely proportional to the thickness of the active layer; therefore the capacitance is lower for thicker active layers.
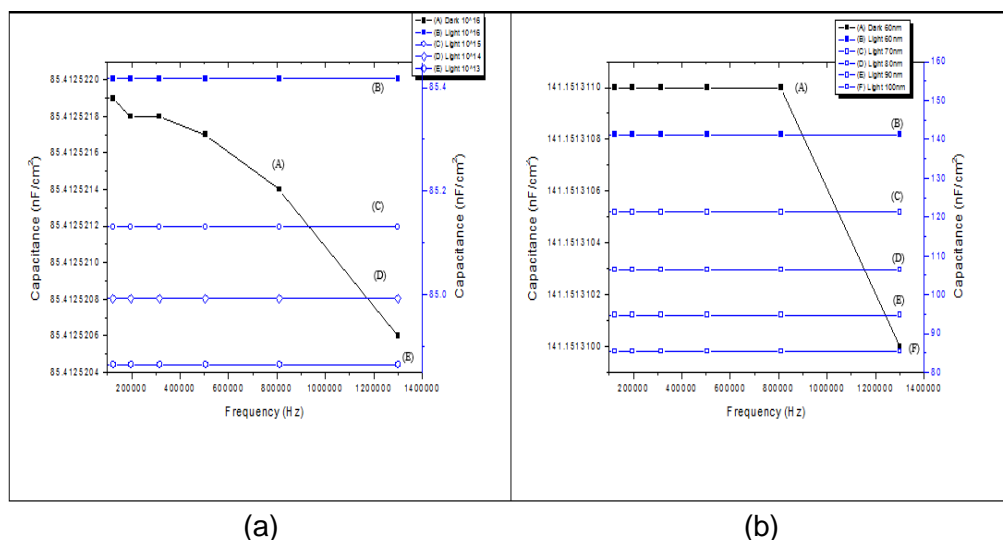
Figure 6. (a) C-f characteristic for every concentration, b) C-f characteristic at every thickness

From the capacitance – frequency (C-f) result shown in Figure 6 (a), it can be seen that the highest capacitance value is when the concentration is at 1.0 x 1016 cm^{-3} and under illumination. The capacitance is not really affected by carrier concentration as the frequency increases and it shows that even the concentration increases from 1.0 x 1013 cm^{-3} to 1.0 x 1016 cm^{-3}, the capacitance range did not change a lot. (B) shows the highest capacitance value around 85.4125 nF/cm^2 while (E) has the lowest capacitance value at 84.832 nF/cm^2. The capacitance value remains constant when the active layer is under illumination occurs due to fixed temperature in the simulation program.

Figure 6 (b) shows the effect of the active layer's thickness towards the capacitance of P3HT: Graphene solar cell. The capacitance decrease as the active layer's thickness increases. The thickness of 60 nm has the highest capacitance value while a thickness of 100 nm has the lowest. As seen in Figure 6 (b), the capacitance of P3HT:Graphene stays static as the frequency increases but the capacitance value between (B) and (F) has a larger gap compared to the one in Figure 6 (a). This shows that the thickness has a greater effect towards the solar cell's capacitance value than the carrier's concentration. As shown in Figure 5 (a), a decrease in capacitance when the frequency increases. For all thickness under illumination, the graph is actually quite the same as (A) but because the decrease of capacitance is really small, it seen as a straight line. From the graph, it can be concluded that the thickness of the thin film has a small effect on the capacitance as the frequency increases because capacitance is mainly affected by the temperature [19]. The reason why the capacitance decreases when the active layer is thicker is because the distance between two electrodes of the solar cells increase, which cause the capacitance to slowly decrease.

CONCLUSION

A simulation on the effect of the thickness and concentration towards the solar cell's characterization has successfully been done. It can be concluded that the thicker and the more higher the concentration, the higher the power conversion efficiency. When the thickness and the concentration of P3HT is increased, the total of carrier concentration increases and will lead to a higher photocurrent.

As for C-V characterization results, P3HT at 100 nm and the concentration at 1.0 x 10^{16} cm^{-3} shows the best results out of all the thickness and concentration of P3HT layer. This is because the peak at C-V characteristic appears really clearly at both results. Besides that, at forward bias, the capacitance value shows a strong sign that the minority charge carriers plays an important role.

For C-f measurements, it can be concluded that the thin film's thickness & concentration have a little effect on the capacitance as the frequency increases. The capacitance decrease as the thickness of the active layer increases due to the increase of distance from the two electrodes. The thickness of the active layer will separate the electrodes even more, which leads to the decrease in capacitance.

REFERENCES

[1] Yu, G., Gao, J., Hummelen, J.C., Wudl, F. and Heeger, A.J., (1995). Polymer photovoltiac cells: Enhanced efficiencies via a network of internal donor-acceptor heterojunctions. *Science*, **270**(5243): 1789–1791.

[2] Xue, J., Uchida, S., Rand, B.P. and Forrest, S.R., (2004). Asymmetric tandem organic photovoltaic cells with hybrid planar-mixed molecular heterojunctions. *Applied Physics Letters*, **85**(23): 5757-5759.

[3] Shaheen, S.E., Brabec, C.J., Sariciftci, N.S., Padinger, F., Fromherz, T. and Hummelen, J.C., (2001). 2.5% efficient organic plastic solar cells. *Applied Physics Letters*, **78**(6):841-843.

[4] Liu, Q., Liu, Z., Zhang, X., Yang, L., Zhang, N., Pan, G., Yin, S., Chen, Y. and Wei, J., (2009). Polymer photovoltaic cells based on solution-processable graphene and P3HT. *Advanced Functional Materials*, **19**(6): 894-904.

[5] Saini, V., Abdulrazzaq, O., Bourdo, S., Dervishi, E., Petre, A., Bairi, V.G., Mustafa, T., Schnackenberg, L., Viswanathan, T. and Biris, A.S., (2012). Structural and optoelectronic properties of P3HT-graphene composites prepared by in situ oxidative polymerization. *Journal of Applied Physics*, **112**(5): 54327–54329.

[6] Saini, V., Li, Z., Bourdo, S., Dervishi, E., Xu, Y., Ma, X., Kunets, V.P., Salamo, G.J., Viswanathan, T., Biris, A.R. and Saini, D., (2009). Electrical, optical, and morphological properties of P3HT-MWNT nanocomposites prepared by in situ polymerization. *The Journal of Physical Chemistry C*, **113**(19): 8023-8029.

[7] Tremolet de Villers, B., Tassone, C.J., Tolbert, S.H. and Schwartz, B.J., (2009). Improving the reproducibility of P3HT: PCBM solar cells by controlling the PCBM/cathode interface. *The Journal of Physical Chemistry C*, **113**(44): 18978-18982.

[8] Wang, G., Hirasa, T., Moses, D. and Heeger, A.J., (2004). Fabrication of regioregular poly (3-hexylthiophene) field-effect transistors by dip-coating. *Synthetic metals*, **146**(2): 127-132.

[9] Chang, Y.W., Yu, S.W., Liu, C.H. and Tsiang, R.C.C., (2010). Morphological and optoelectronic characteristics of nanocomposites comprising graphene nanosheets and poly (3-hexylthiophene). *Journal of nanoscience and nanotechnology*, **10**(10): 6520-6526.

[10] Steirer, K.X., Reese, M.O., Rupert, B.L., Kopidakis, N., Olson, D.C., Collins, R.T. and Ginley, D.S., (2009). Ultrasonic spray deposition for production of organic solar cells. *Solar Energy Materials and Solar Cells*, **93**(4): 447-453.

[11] Moulé, A.J., Bonekamp, J.B. and Meerholz, K., (2006). The effect of active layer thickness and composition on the performance of bulk-heterojunction solar cells. *Journal of applied physics*, **100**(9): 094503.

[12] Iwan, A. and Chuchmała, A., (2012). Perspectives of applied graphene: Polymer solar cells. *Progress in Polymer Science*, **37**(12): 1805-1828.

[13] Mallajosyula, A.T., Iyer, S.S.K. and Mazhari, B., (2012). Capacitance–voltage characteristics of P3HT: PCBM bulk heterojunction solar cells with ohmic contacts and the impact of single walled carbon nanotubes on them. *Organic Electronics*, **13**(7): 1158-1165.

[14] Van Mensfoort, S.L.M. and Coehoorn, R., (2008). Determination of injection barriers in organic semiconductor devices from capacitance measurements. *Physical review letters*, **100**(8): 086802.

[15] Zhang, J.W., He, Y., Chen, X.Q., Pei, Y., Yu, H.M., Qin, J.J. and Hou, X.Y., (2015). Study on the basic capacitance–voltage characteristics of organic molecular semiconductors. *Organic Electronics*, **21**: 73-77.

[16] Tripathi, D.C. and Mohapatra, Y.N., (2013). Diffusive capacitance in space charge limited organic diodes: Analysis of peak in capacitance-voltage characteristics. *Applied Physics Letters*, **102**(25): 253303.

[17] Pahner, P., Kleemann, H., Burtone, L., Tietze, M.L., Fischer, J., Leo, K. and Lüssem, B., (2013). Pentacene Schottky diodes studied by impedance spectroscopy: Doping properties and trap response. *Physical Review B*, **88**(19): 195205.

[18] Lenes, M., Koster, L.J.A., Mihailetchi, V.D. and Blom, P.W.M., (2006). Thickness dependence of the efficiency of polymer: fullerene bulk heterojunction solar cells. *Applied Physics Letters*, **88**(24): 243502.

[19] Zhang, Y., Li, L., Yuan, S., Li, G. and Zhang, W., (2013). Electrical properties of the interfaces in bulk heterojunction organic solar cells investigated by electrochemical impedance spectroscopy. *Electrochimica Acta*, **109**: 221-225.

Controller Design Using Ziegler-Nichols First Method for Air Blower PT326

Mahanijah M. Kamal, Muhammad H.A. Halim

Faculty of Electrical Engineering, Universiti Teknologi MARA, Kompleks Kejuruteraan, 40450, Shah Alam, Selangor DE, Malaysia.
(*corresponding Author: mahani724@salam.uitm.edu.my)

Abstract   In this work, two types of controller are designed for the nonlinear air blower system PT326 used in the Instrumentation Laboratory Faculty Electrical Engineering, UiTM Shah Alam. This work begins with the collection of data from the experimental work. Once the S-shape of the system response is obtained, the procedure of getting the process dead time, τ_D and time constant τ_c was applied to the S-shape form. By determining these two values, the optimum values of PI and PID controllers can be calculated. From the acquired data, the simulation model is developed in MATLAB/Simulink R2013a software using the transfer function obtained from the open-loop control system. The modelling system is based on the transfer function of open-loop air blower system PT326 before the design state of finding a suitable controller can be suggested. The controller design of PI and PID was obtained using the first method Ziegler-Nichols tuning rules. The results from the simulation are reliable and satisfactory. It shows that the Ziegler-Nichols first tuning rules can be applied in designing the PI and PID controller based on S-shape response obtained in open-loop test.

INTRODUCTION

In process industries, temperature control plays an important role in order to produce a good quality end product. The temperature control of different systems is required and the rates of reaction are controlled by heating and cooling the reactants. For instance in the plastic injection moulding process as in [1], the temperature in each temperature zone must be appropriately set and precisely controlled. The PID controllers are still widely used in the process industries even though control theory has been developed significantly since they were first used decades ago [1]. In 1942, Ziegler-Nichols presented a tuning formula [2-3], based on time response and open-loop response rate of the system.

The most frequently used experimental methods are the Ziegler-Nichols open-loop and closed-loop design methods. In this work, the first method of Ziegler-Nichols is used to monitor the performance of the air blower system PT326. Open-loop proses identification is the most common method used to obtain the information of the process dead time and also the process response rate. Normally the system response is in the form of S-shape by drawing a tangent line on the response curve where the optimum values of PID controller can be attained. Nowadays, there are a lot of publications on the tangent technique as well as on the PID controller tuning. The analysis of open-loop response using the concept of S-shape or tangent method has been reformulating by Ishak and Hussain [4] where they have

come out with a new algorithm, which offers easier and faster calculation on the process response. Further experimental study has been conducted by Ishak and Hussain [5] where they designed a PID controller to control a flow of water to verify their proposed technique. Later, the concept of open-loop response has been implemented on a PID controller tuning using the Ziegler-Nichols technique by Kamaruddin et al [6] for a glycerine bleaching process whereas Hambali et. al [7-9] used this technique for flow, temperature and also pressure based on tangent method for various PID tuning rules. The objective of this work is to design a suitable controller for air blower system PT326. Hence, a model system of PT326 has been developed and the design of PI and PID controller based on Ziegler-Nichols first method was simulated. Observation was made to monitor the response of both in order to determine which one is suitable controller for air blower process PT326.

METHODOLOGY

In the work on temperature control, a simple laboratory experiment using air blower systems PT326 as in Figure 1 was conducted. The PT326 is a self-contained process and control equipment where it has basic characteristic of large plant with transfer lag, system response, enable distance/velocity lag and proportional control. This mimics the actual industrial process that utilizes the temperature parameter as the control element where the temperature of the air blower system is maintained at a certain level. In PT326 system it only allows the gain to be adjusted in order to achieve the best characteristic outputs in terms of peak time, settling time and steady state error.   This is not sufficient to control the temperature of the air blower system. Therefore based on the open-loop test, a new controller is proposed using Ziegler-Nichols tuning rules in order to improve the output characteristics.

The signal generator is set with amplitude of 2V peak to peak with temperature set at 35°C. Initially the open loop test on frequency response with sinusoidal input signal is carried out at starting frequency of 0.01 Hz to model the process in order to obtain the transfer function of the process. The tuning of both rules are carried out to obtain the proportional constant, Kp, integral constant KI, and derivative constant, KD. These constants are derived from τ_D and τ_c obtained from the output response of an open loop test with step input using Ziegler-Nichols first method where S-shape response was obtained. The constant values are used to simulate the PI and PID controller and the output characteristics are observed.
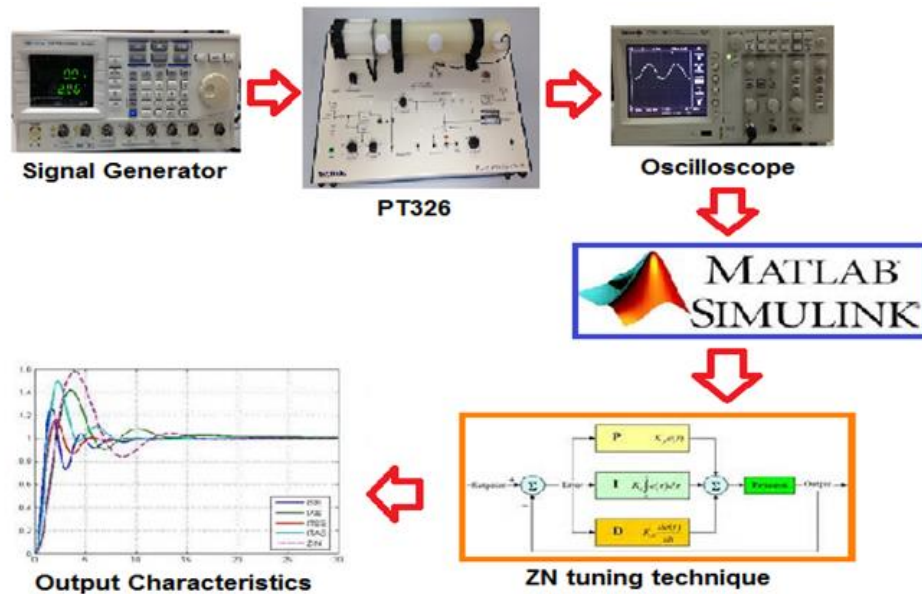
Figure 1. The Methodology Process

RESULTS AND DISCUSSION

Several methods are available for designing PID controller. The most frequently used experimental methods are Ziegler-Nichols open-loop and closed loop design methods. However in this work, the work is focusing on Ziegler-Nichols open-loop first method where the system response to a step input is in S-shape form. Figure 2 shows the response curve of process trainer PT326 of air blower system in S-shape where the design of PI and PID controller can be developed.
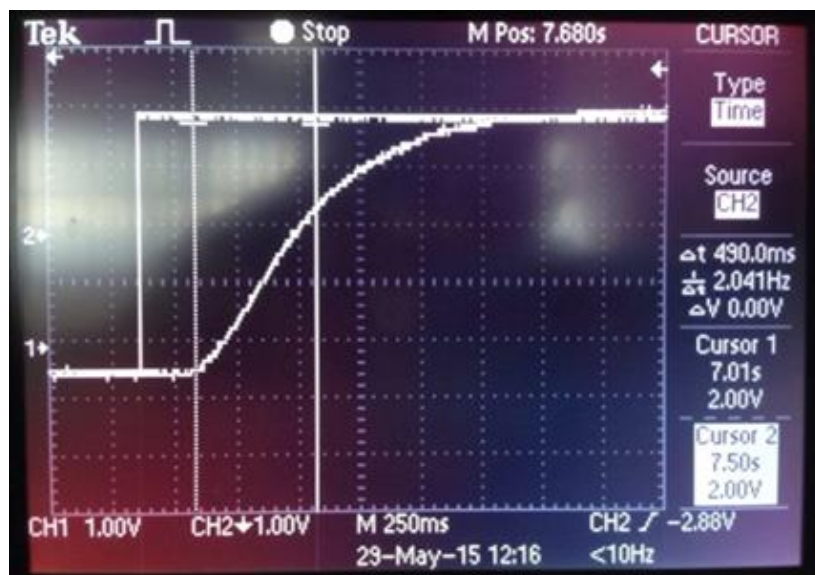

Figure 2. The S-shape response using Ziegler-Nichols first method

The design procedures are:
1. Obtain an open-loop step response from the experiment.
2. Draw the tangent line on the response curve.
3. Using the cross-points of the tangent with x-axis and with the steady-state output line to determine т_D and т_c.
4. PID controller tuning design can be used using the formulae stated in Table 1.

Table 1. Ziegler-Nichols First Method Open-Loop Tuning Parameters

Controllers	Kc	τ_I	τ_D
P	$\dfrac{\tau_c}{\tau_D}$	∞	0
PI	$0.9\dfrac{\tau_c}{\tau_D}$	$\dfrac{\tau_D}{0.3}$	0
PID	$1.2\dfrac{\tau_c}{\tau_D}$	$2\tau_D$	$0.5\tau_D$

By applying the above procedures, the time delay, т_D and time constant, т_c can be determined. The tangent line at the inflection point of S-shape curve determining the intersections of the tangent line with the time axis and the voltage axis. From the graph as in Figure 2, the value of т_D =0.27s and т_c = 0.55s was obtained. Once the value of т_D =0.27s and т_c = 0.55s are known, the next step is to design the suitable controller for air blower system PT326 using the parameters as stated Table 1.

**Table 2.** The Parameters of P, Pi And Pid Controller

Controllers	Kc	τ_I	τ_D
P	2.04	∞	0
PI	1.833	0.9	0
PID	2.44	0.54	0.135

Table 2 shows the value of P controller, PI controller and PID controller design using Ziegler-Nichols first method. The air blower system PT326 only consists of P controller. Therefore, to analyse the parameters in TABLE 2, MATLAB/Simulink R2013a is used to model the air blower system PT326. Based on the experimental results, the transfer function of air blower system PT326 was obtained. The open-loop transfer function is given as in Eq. (1).

$$G(s) = \frac{0.54}{(s+0.36)(s+1.5)} \qquad \text{Eq. (1)}$$

The calculations obtained in Table 2 are used as the parameters setting in the simulation model connected with the transfer function of process trainer PT326 as in Eq. (1). Figure 3 shows the MATLAB/Simulink model constructed where the step response is injected as the input signal.
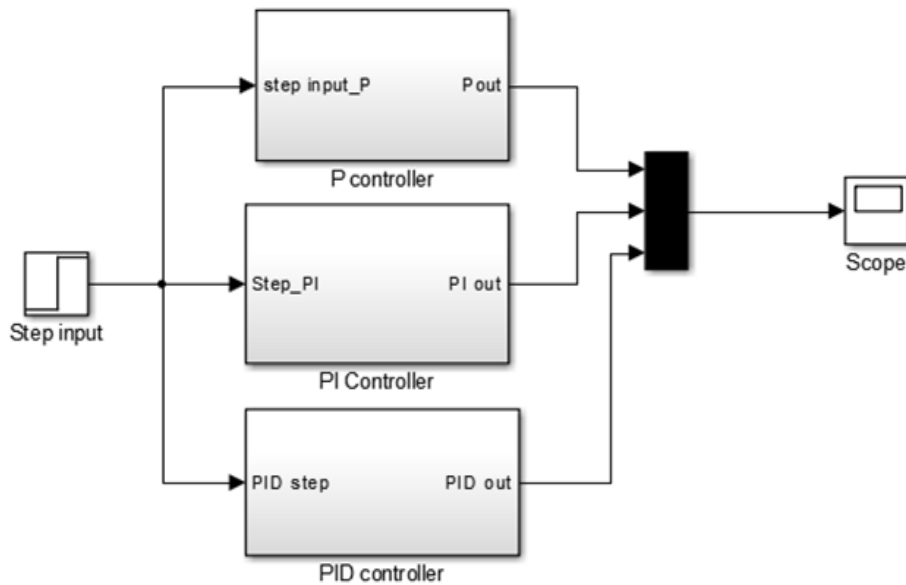

Figure 3. The Model of Pt326 In Simulink Model

Figure 4 shows the simulation result of three controllers: P controller, PI controller and PID controller. From the observation, with P controller the output cannot achieved the steady-state response whereas PI controller has the ability to improve the steady state error while combination of PID will improve the transient response in terms of settling time, ts, peak time, tp and steady state error. Based on the output response, the rise time, tr of PID controller is faster than PI controller. However, PID controller has a higher overshoot compared with PI controller. Both controllers achieved SSE which indicate that the final response of process trainer PT326 will be at a constant value at certain length of time.
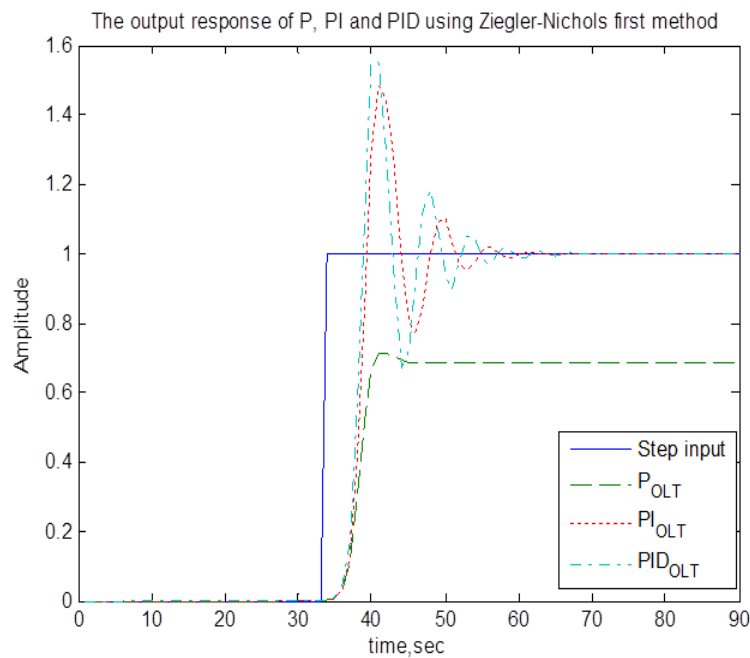
Figure 4. The Controller Response Based On Ziegler-Nichols First
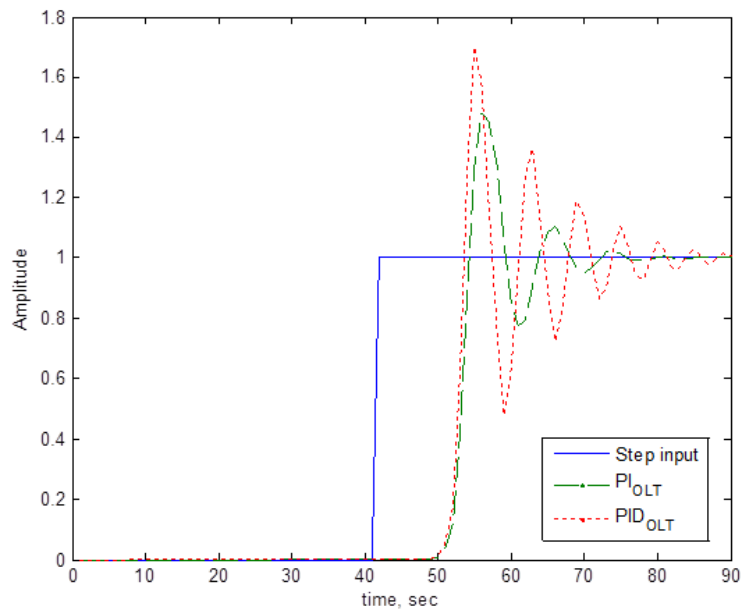
Figure 5. The Effect of Integrator In Pid Controller

In order to analyse the effect of integrator towards the process response of air blower PT326, the value of integral in the PID controller has been changed from τ_I=0.54 to τ_I=0.48. Referring to Figure 5, if the value of integral in the PID controller is lesser than the original, the response oscillate more before it achieved steady state. Even though the output response oscillates more compared to PID controller in Figure 4, the response will still achieve steady-state condition. Only the time taken is longer from the other signal. However the time taken is longer from the original response.
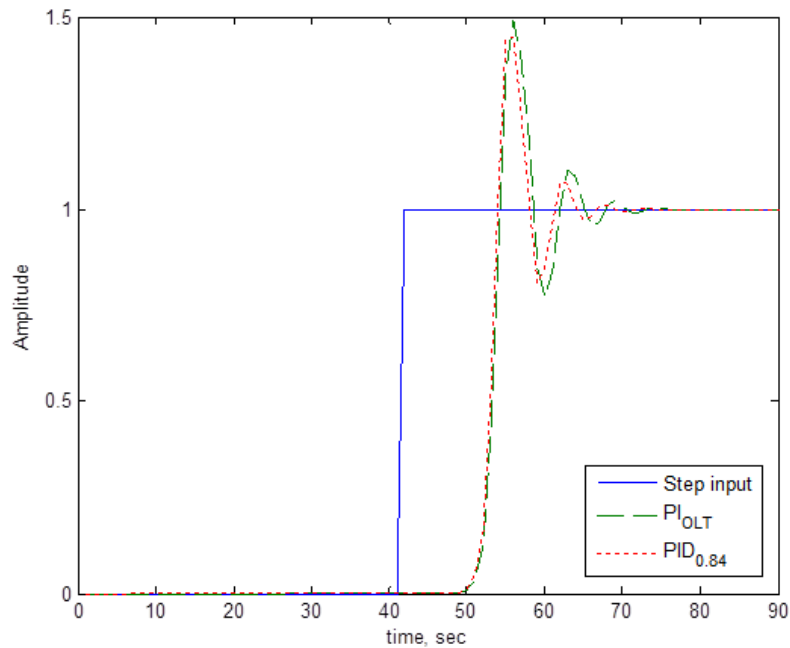
Figure 6. The Effect of Integrator In Pid Controller

Again, the value of integral in the PID controller has been changed from τ_I=0.54 to τ_I=0.84. Based on Figure 6 it shows that the response of PID controller is almost similar with PI controller output. If the value of integral in PID controller is higher than the value from the open-loop test, the overshoot has reduced and it achieved steady state faster compared with the PID controller response in Figure 4 and Figure 5.

CONCLUSION

A simulation on the effect of the thickness and concentration towards the solar cell's characterization has successfully been done. It can be concluded that the thicker and higher the concentration, the higher the power conversion efficiency. When the thickness and the concentration of P3HT is increased, the total of carrier concentration increases and will lead to a higher photocurrent.

As for C-V characterization results, P3HT at 100nm and the concentration at 1.0 x 1016 cm-3 shows the best results out of all the thickness and concentration of P3HT layer. This is because the peak at C-V characteristic appears really clearly at both results. Besides that, at forward bias, the capacitance value shows a strong sign that the minority charge carriers plays an important role.

For C-f measurements, it can be concluded that the thin film's thickness & concentration have a little effect on the capacitance as the frequency increases. The capacitance decrease as the thickness of the active layer increases due to the increase of distance from the two electrodes. The thickness of the active layer will separate the electrodes even more, which leads to the decrease in capacitance.

REFERENCES

[1]   Lu, C.H. and Tsai, C.C., (2001). Adaptive decoupling predictive temperature control for an extrusion barrel in a plastic injection molding process. *IEEE Transactions on Industrial Electronics.* **48**(5):.968-975.

[2]   Zhuang, M. and Atherton, D.P., (1993), May. Automatic tuning of optimum PID controllers. In *IEE Proceedings D-Control Theory and Applications.* **140**(3): 216-224

[3]   Åström, K.J. and Hägglund, T., (1995). PID controllers: theory, design, and tuning. *Library of Congress Cataloging-in-Publication Data*

[4]   Xue, D., Chen, Y. and Atherton D.P. (2007). Linear Feedback Control. *Society of Industrial Mechatronics and Applied Mathematics.*

[5]   Ishak, A.A. and Hussain, M.A., (1998). Open-loop process identification: Reformulation of response rate calculation. In *Proceeding of Regional Symposium on Chemical Engineering.* pp. 1-5.

[6]   Ishak, A.A. and Hussain, M.A., (1998). Reformulation of the tangent method for PID controller tuning. In *TENCON 2000. Proceedings,* pp. 484-488.

[7]   Kamaruddin, N., Janin, Z., Yusuf, Z. and Taib, M.N., (2009), November. PID controller tuning for glycerin bleaching process using well-known tuning formulas-a simulation study. In *Industrial Electronics, 2009. IECON'09. 35th Annual Conference of IEEE.* pp. 1682-1686.

[8]   Hambali, N., Zaki, M.N.K. and Ishak, A.A., (2012), November. Reformulated tangent method of various PID controller tuning for air pressure control. In *Control System, Computing and Engineering (ICCSCE), 2012 IEEE International Conference on.* pp. 17-22.

[9]   Hambali, N., Masngut, A., Ishak, A.A. and Janin, Z., (2014), November. Process controllability for flow control system using Ziegler-Nichols (ZN), Cohen-Coon (CC) and Chien-Hrones-Reswick (CHR) tuning methods. In *Smart Instrumentation, Measurement and Applications (ICSIMA), 2014 IEEE International Conference on.* pp. 1-6.

21-Level Cascaded H-Bridge Multilevel Inverter for Dual-Power PV-Grid Energy System

Intan Rahayu Ibrahim, Ahmad Maliki Omar, Zakaria Hussain, Mohd Najib Mohd Hussain, Norsalwa Damanhuri and Norazlan Othman
Faculty of Electrical Engineering, Universiti Teknologi MARA, Shah Alam, Selangor DE, Malaysia
(*corresponding author: intan121@ppinang.uitm.edu.my)

Abstract   In the dual-power PV-grid system, the PV-battery system is operated in alternately during the on-demand and off-demand period. The cascaded H-bridge multilevel inverter is preferable in the power converter of the photovoltaic (PV) energy system due to its capability of synthesizing the desired AC voltage from various separate DC sources, low component ratings, and uses less components compared to other multilevel inverters. The cascaded multilevel inverter provides 'stepped' AC waveforms from DC sources and the quality of the outputs strongly related to the number of level of the 'stepped' signals.   Power switches of the inverter are switched at low fundamental frequency to avoid switching and conduction losses. The Selective Harmonics Elimination (SHE) technique was employed to eliminate certain harmonics of the output inverter by optimizing the switching angles of each of the power switch. The paper discusses the 21-level cascaded multilevel inverter implemented in the power converter of the dual-power PV-grid energy system and the switching technique to generate optimized switching angles using modified combination of particle swarm and evolutionary programming methods. The inverter provides 21 levels of 'stepped' AC voltage of 240V, 50Hz with percentage total harmonics distortion (THD) of 3.93 %.

Keywords   Dual-power PV-grid system; cascaded multilevel inverter; selective harmonics elimination (SHE); PV power converter

INTRODUCTION

It is necessary to combine the PV system to other renewable energy sources or a diesel generator to provide uninterruptible power supply [1, 2]. As an alternative, the dual-power PV-grid was introduced. The system combines the PV system with the grid whereby the grid will stand as a backup to the system during the day or during on-demand period. Meanwhile, during the night or off-demand period, the grid will supply the load with PV-battery system as a backup. While providing continuous power supply, the system provides low installation and maintenance cost [3], save the electricity bills by employing the incentive of low off-demand tariff in the dual-tariff system and effortlessly associated in the feed in tariff (FiT) program introduced by the government [4].

The multilevel inverter produced 'stepped' desired AC output voltage waveform from several DC sources [5-7]. The structure allows the inverter to reach high voltages with low harmonic and without the use of transformer and an output filter [8-10]. In absence of any PWM techniques, the switching losses can be avoided [11, 12]. Furthermore, it also does not require an increase in rating of devices if the output voltage and power are increased [12].

There are three prominent types of multilevel inverter which are the diode clamped, flying capacitor and cascaded H-bridge inverters.

Cascaded inverter has been accredited as the best topology for single-phase PV system [10, 12, 13]. By cascading a series of single-phase full-bridge inverter (H-bridge) the desired AC voltage could be synthesized from separate DC sources of battery, solar cells, fuel cells, and many more. In addition to requirement of less number of components which optimizes circuit layout and packaging and less complicated switching technique, the cascaded H-bridge multilevel inverter becomes the ultimate choice of multilevel inverter to be implemented in the standalone PV energy system.

In this paper, the new topology and switching strategy of the 21-level cascaded H-bridge multilevel inverter implemented in the power converter of the dual-power PV-grid energy system is described and discussed.

DUAL-POWER PV-GRID ENERGY SYSTEM

The dual-power PV-grid system is combination of a PV-battery system and a grid system which alternately supplies a load. The transition of power supply from the PV-battery system to the grid system and vice versa is controlled by the switchover circuit as depicted in Figure 1. During the day, the PV energy system will supply the load and in the event of insufficient power supply from the PV array, the battery will make up the shortfall. The battery charging process will automatically occur from the grid whenever the battery voltage falls below a preset value in order to maintain the battery bank at its float voltage. The PV energy system operates as a stand-alone PV energy system with batteries being charge from the PV array. Figure 2 shows the Dual-power PV-grid energy system which is currently installed in Universiti Teknologi MARA, Pulau Pinang, Malaysia.
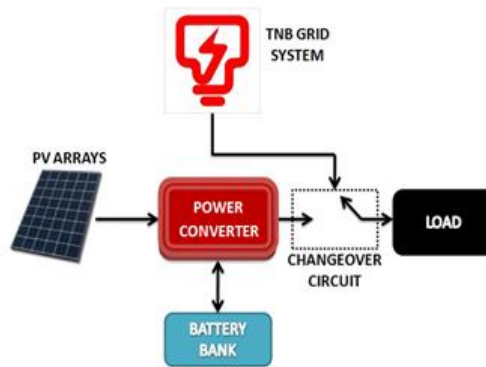
POWER CONVERTER

Basically the power converter system in a standalone PV energy system consists of a DC-DC regulator to regulate an intermittent power from PV, maximum power trackers (MPT) to ensure the maximum energy is obtained from PV cells, a battery converter to protect the battery from overcharging or undercharging and an inverter to convert DC PV power to AC. Figure 3 illustrates the power converter system as proposed in this research. The digital control system is used in the power converter components to enhance reliability and faster response [14].

Topology
In this design, the cascaded H-bridge multilevel inverter as illustrated in the Figure 4 below was used to synthesize 240V, 50Hz AC voltage from five strings of PV modules. By adding a power switches, four diode and two capacitors in front of the H-bridge as in Figure 5, the H-bridge output level could be increased from three to five. Each of the H-bridge produces 5 levels output of 1/2 VDC, VDC, 0, -1/2 VDC and –VDC as depicted in Figure 6.

By cascading 5 H-bridges, the higher voltage levels can be obtained and the resultant output voltage is the sum of voltages of separate DC sources supplying the H-bridge. Table 1 summarizes the voltage level corresponding to conducting power switches of the proposed cascaded H-bridge multilevel inverter. Figure 7 demonstrates the hardware construction of the inverter.

Figure 1. Dual-power PV-grid Energy System

Figure 2. Dual-power PV-grid Energy System Currently Installed in UiTM Pulau Pinang, Malaysia
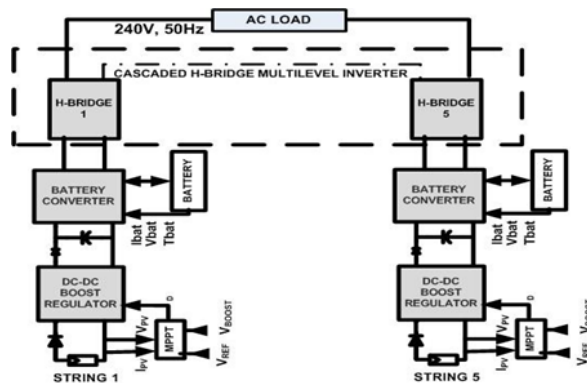
**Figure 3.** Power Converter for Dual-power PV-grid Energy System

Table 1.   Active Power Switches and Output Voltage Levels

| Active Switches	Output Voltage
S11,S41,S12,S42,S13,S43,S14,S44,S15,S45	5VDC
S11,S14,S12,S42,S13.S43,S14,S44,S45,S55	9/2VDC
S11,S41,S12,S42,S13,S42,S14,S44	4VDC
S11,S41,S12,S42,S13,S43,S44,S45	7/2VDC
S11,S41,S12,S42,S13,S43	3VDC
S11,S41,S12,S42,S43,S53	5/2VC
S11,S41,S12,S42	2VDC
S11, S41,S42,S52	3/2VDC
S11, S41	VDC
S41, S51	1/VDC
All Power Switches are Inactive	0
S21,S51	-1/2VDC
S21,S31	-VDC
S21,S31,S22,S25	-3/2VDC
S21,S31,S22,S32	-2VDC
S21,S31,S22,S32,S23.S53	-5/2VDC
S21,S31,S22,S32,S23,S33	-3VDC
S21,S31,S22,S32,S23,S33,S24,S54	-7/2VDC
S21,S31,S22,S32,S23,S33,S24,S34	-4VDC
S21,S31,S22,S32,S23,S33,S24,S34,S25,S55	-9/2VDC
S21,S31,S22,S32,S23,S33,S24,S34,S25,S35	-5VDC

Switching Strategy - Selective Harmonics Elimination (SHE)

As the In SHE, the switching angles of power switches are pre-calculated and pre-defined to eliminate certain harmonic orders [15]. In order to eliminate, fifth, seventh and eleventh harmonics, and to maintain the fundamental voltage to 100%, transcendental equations with 10 unknowns as shown below need to be solved.

- $[\cos(\theta_1) + \cos(\theta_2) + \cos(\theta_3) \ldots + \cos(\theta_{10})] = 5M$
- $[\cos(5\theta_1) + \cos(5\theta_2) + \cos(5\theta_3) \ldots + \cos(5\theta_{10})] = 0$
- $[\cos(7\theta_1) + \cos(7\theta_2) + \cos(7\theta_3) \ldots + \cos(7\theta_{10})] = 0$
- $[\cos(11\theta_1) + \cos(11\theta_2) + \cos(11\theta_3) \ldots + \cos(11\theta_{10})] = 0$
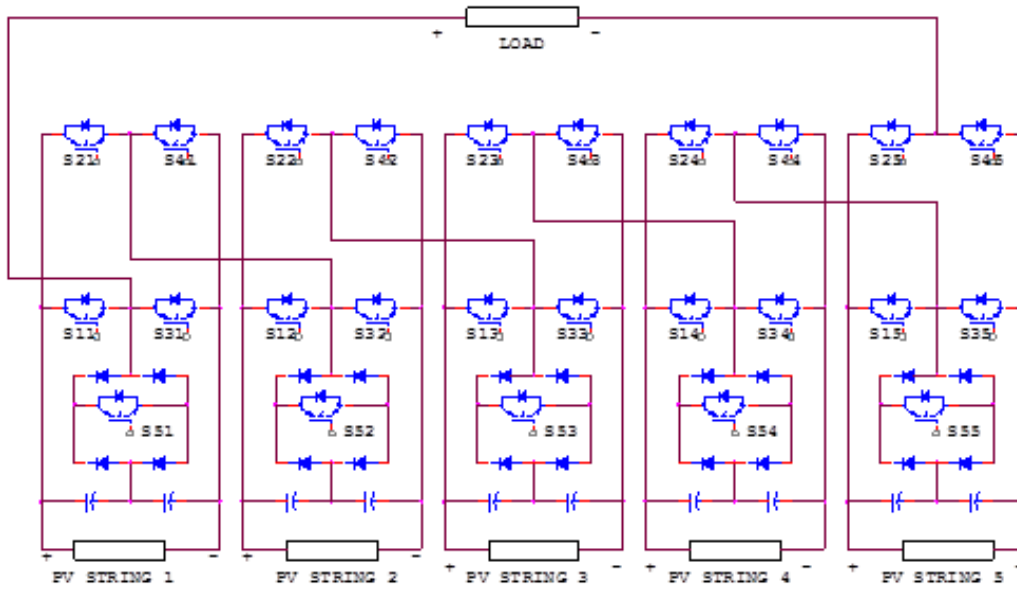
Figure 4. Proposed Reduced Switch Increased Level of Cascaded Multilevel Inverter
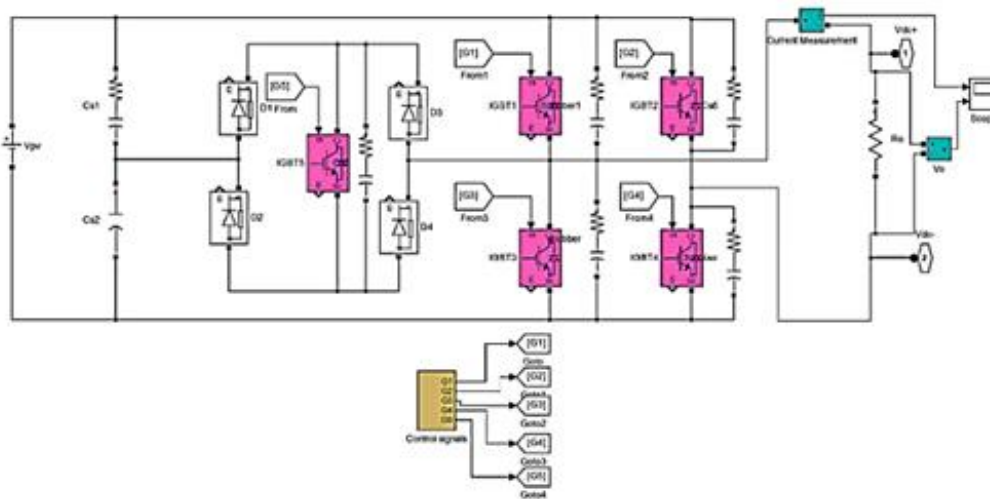
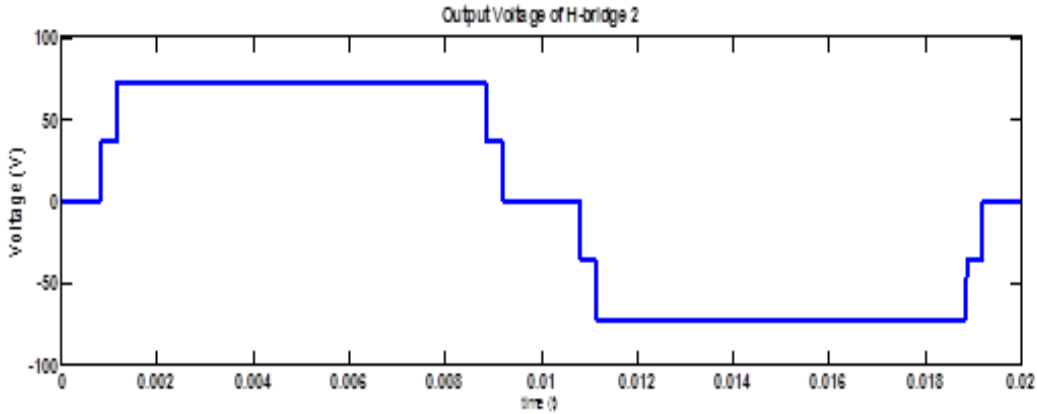**Figure 5.** H-bridge With Added Components to produce 5-level Output

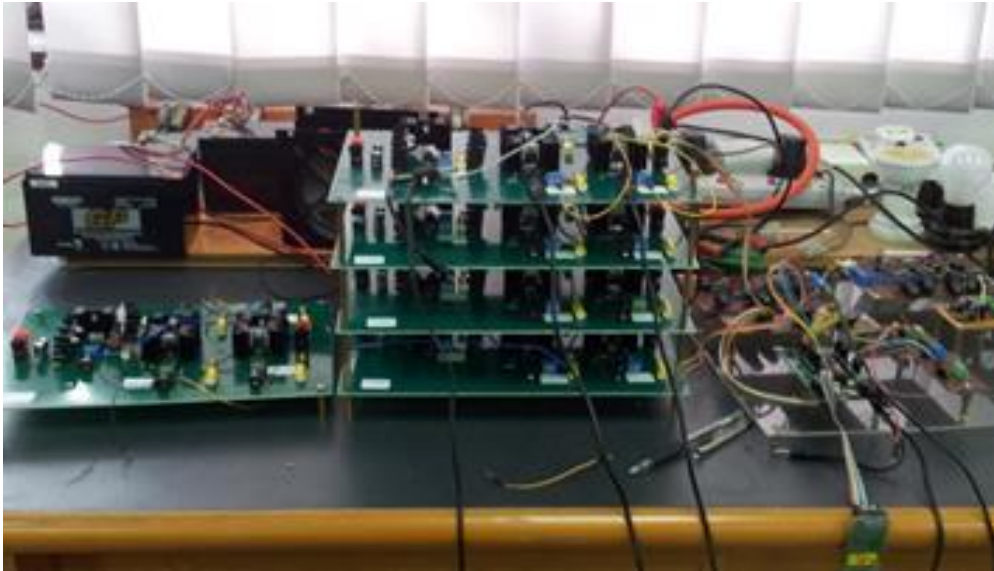**Figure 6.** The 5-level Output Waveform of the H-bridge

Figure 6. Hardware construction of the 21-level cascaded H-bridge multilevel inverter

The equations could be solved using Newton-Raphson method, mathematical theory of resultant, genetic algorithm (GA), particle swarm optimization (PSO), or using evolutionary programming (EP).

Modified Particle Swarm Optimization Technique
In this research, modified PSO is used to solve transcendental equations and produce optimized value of switching angles to be used in the cascaded multilevel inverter in order to reduce fifth, seventh, ninth and eleventh harmonics. Random numbers generated by PSO sometimes cannot satisfy requirement of switching angles for multilevel inverter such as θ_1 should less than θ_2. Therefore, the random angle generations was modified using EP method.

As summary, the method was adapted by following the step below:-
o Initialize population size, modulation index, maximum iteration and iteration counter.
o Generate random switching angles for each particle which fulfill the criteria:-

- Each switching angle lays on the specific range so that $\theta_1 < \theta_2 < \theta_3 < ...\pi$.
- Each particle generates minimum fifth, seventh, ninth and eleventh harmonics.
- Generate the initial conditions of each particle ($0<\theta<\pi$). Initial values are computed based on manual estimation.
  - Evaluate particles using fitness function of harmonic minimization problem.
  - Update the personal best position of the particles. If the personal best of the particles is better than the position of global best, replace global best with the best position of the personal best.
  - Update the velocity and position vector.
  - Termination criteria – if iteration reaches maximum iteration, stop the iteration, otherwise increase the iteration counter and repeat step 3, 4, and 5.

Table 2 tabulates switching angles generated by proposed modified PSO and simulated percentage of THD produced by the inverter. Figure 8 shows output waveforms of each of H-bridge in the multilevel inverter which produces the 21-level "stepped" resultant output waveform in the cascaded topology. The topology will *produce (4 x n +1)* level of 'stepped' sinusoidal voltage. For *n* = number of PV string = *5*, Figure 9 displays the computed percentage THD of the output waveform.
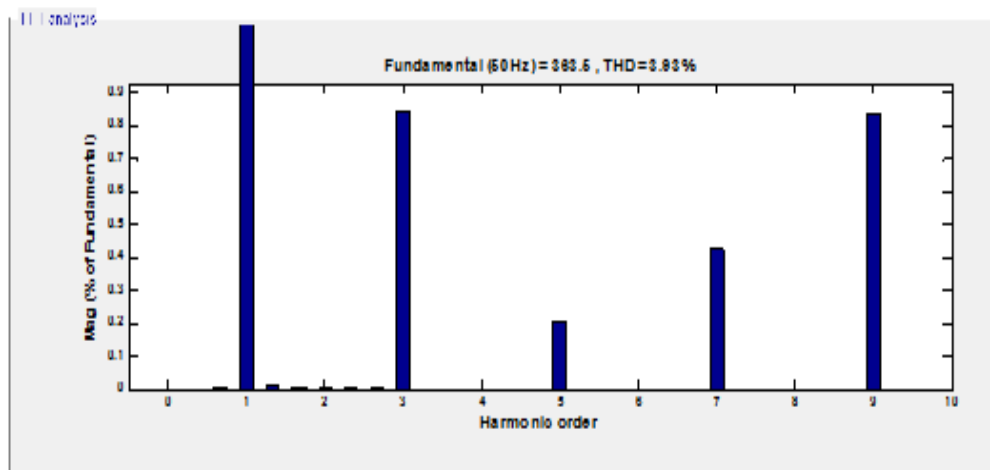
Table 2. Switching Angles Generated by the Particle Swarm Optimization Technique.

Switching Angles (°)									
θ_1	θ_2	θ_3	θ_4	θ_5	θ_6	θ_7	θ_8	θ_9	θ_{10}
□□□□	□□□□	□□□□□	□□□□□	□□	□□	□□	□□	□□□□□	□□□□□
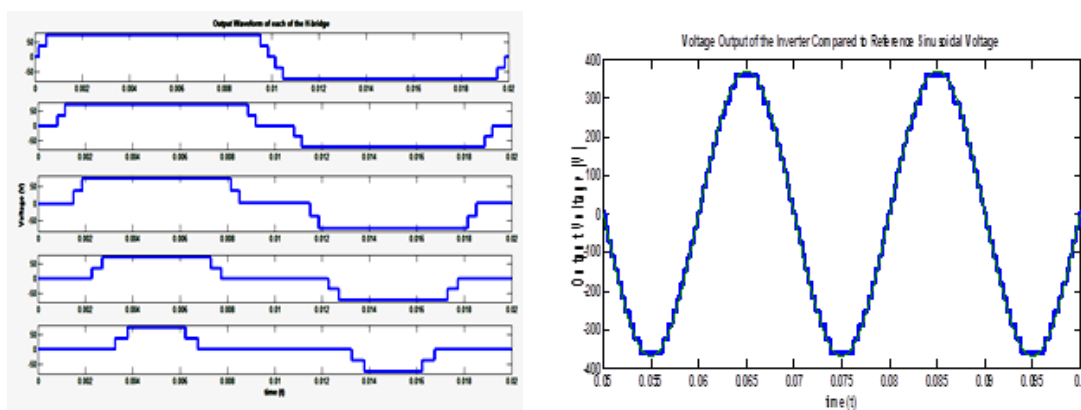
Figure 8. Output waveforms for each of H-bridge and the 21-level 'Stepped' AC voltage generated by 5 Cascaded H-bridge

Figure 9. %THD of Output Voltage of the 21-level Cascaded H-bridge Multilevel Inverter

CONCLUSION

The dual-power PV-grid system was introduced to reduce the capital installation cost of the PV energy system by reducing the number of PV panels and batteries. Moreover, the cascaded H-bridge multilevel inverter was utilized in the power converter of the photovoltaic (PV) energy system due to its capability of synthesizing the desired AC voltage from various separate DC sources with low component ratings and less components. In this research, 21 power switches are switched at low frequency with optimized switching angles generated by modified PSO and EP technique to produce 21-level 'stepped' AC waveforms from DC sources. Selected harmonics components namely fifth, eleventh, ninth and eleventh are effectively suppressed using SHE switching strategy and results in generating inverter output of 240V, 50Hz AC voltage with percentage of total harmonics distortion (THD) of 3.93 %.

REFERENCES

[1]   Nema, P., Nema, R.K. and Rangnekar, S., (2009). A current and future state of art development of hybrid energy system using wind and PV-solar: A review. *Renewable and Sustainable Energy Reviews*, 13(8): 2096-2103.

[2]   Paska, J., Biczel, P. and Kłos, M., (2009). Hybrid power systems–An effective way of utilising primary energy sources. *Renewable Energy*, 34(11): 2414-2421.

[3]   International Energy Agency, Management of Storage Batteries used in Stand-Alone Photovoltaic Power Systems - Report-IEA-PVPS-T3-10. (2002). *International Energy Agency (IEA).*

[4]   Muhammad-Sukki, F., Ramirez-Iniguez, R., Abu-Bakar, S.H., McMeekin, S.G., Stewart, B.G. and Chilukuri, M.V., (2011), June. Feed-In Tariff for solar PV in Malaysia: Financial analysis and public perspective. In *Power Engineering and Optimization Conference (PEOCO), 2011 5th International,* pp. 221-226.

[5]   Seyezhai, R. and Mathur, B.L., (2008), September. Hybrid cascaded H-bridge multilevel inverter for fuel cell power conditioning systems. In *Universities Power Engineering Conference, 2008. UPEC 2008. 43rd International,* pp. 1-5.

[6]   Adithya, S.N., (2014), January. Study of Multilevel Sinusoidal PWM methods for cascaded h-bridge multilevel inverters. In *Electrical Energy Systems (ICEES), 2014 IEEE 2nd International Conference on,* pp. 249-254.

[7] Ibrahim, I.R., Omar, A.M., Hussain, Z., Hussain, M., Najib, M., Noor, M. and Zaliha, S., (2014). Dual-Power PV-Grid Energy System-An Alternative to the Off-Grid PV Energy System. In *Advanced Materials Research,* 960: 1531-1535.

[8] Calais, M., Agelidis, V.G. and Dymond, M.S., (2001). A cascaded inverter for transformerless single-phase grid-connected photovoltaic systems. *Renewable Energy*, 22(1): 255-262.

[9] Gupta, K.K., Ranjan, A., Bhatnagar, P., Sahu, L.K. and Jain, S., (2016). Multilevel inverter topologies with reduced device count: A review. *IEEE Transactions on Power Electronics*, 31(1): 135-151.

[10] Babaei, E. and Laali, S., (2015). Optimum structures of proposed new cascaded multilevel inverter with reduced number of components. *IEEE Transactions on Industrial Electronics*, 62(11): 6887-6895.

[11] Lai, J.S. and Peng, F.Z., (1996). Multilevel converters-a new breed of power converters. *IEEE Transactions on industry applications*, 32(3): 509-517.

[12] Lai, Y.S. and Shyu, F.S., (2002). Topology for hybrid multilevel inverter. *IEE Proceedings-Electric Power Applications*, 149(6): 449-458.

[13] Mohammadi, H.R. and Akhavan, A., (2014), June. A new adaptive selective harmonic elimination method for cascaded multilevel inverters using evolutionary methods. In *Industrial Electronics (ISIE), 2014 IEEE 23rd International Symposium on,* pp. 1484-1489.

[14] Ibrahim, I.R., Omar, A.M. and Hussain, Z., (2013), June. Control strategy of power converter system in the dual-power PV-grid system energy utilizing cascaded multilevel inverter. In *Industrial Electronics and Applications (ICIEA), 2013 8th IEEE Conference on,* pp. 848-853.

[15] Marzoughi, A., Imaneini, H. and Moeini, A., (2013). An optimal selective harmonic mitigation technique for high power converters. *International Journal of Electrical Power & Energy Systems*, 49: 34-39.

Compression Behavior of Thin Walled Tubular Structures under Dynamic Buckling

Girija Kumari Sethy and Raghu V. Prakash
Department of Mechanical Engineering, Indian Institute of Technology Madras, Chennai 600036, India
(*corresponding author: raghuprakash@iitm.ac.in)

Abstract   Strain, strain rate and temperature are the key parameters in the deformation characterization of thin walled structures subjected to high strain rate loading. The two contradictory phenomena, viz., strain hardening and thermal softening take place during high strain rate deformation. Proper material model should be used in the numerical analysis for better prediction of the actual deformation behaviour. Understanding the effect of these variables in case of dynamic progressive buckling is essential to understand and improve the energy absorption capability of the structures. Numerical simulation and validation of compression response of an aluminum tubular member is performed using LS-DYNA® explicit solver. Johnson-cook constitutive model is used in the present work which incorporates strain hardening and thermal softening at high strains. The results of a parametric study aimed at understanding the crushing force profile and energy absorption pattern at high strain rates are presented.

Keywords   Thin-walled structures; Progressive buckling; Strain hardening; Thermal softening

INTRODUCTION

Thin walled components absorb energy through a progressive axial collapse which is an efficient mode of energy absorption. Considerable work has been done to study the deformation behaviour of thin walled structures to understand their energy absorption mechanisms during progressive buckling [1-3]. Deformation of thin walled extrusions subjected to impact depends on several factors such as:

- Material properties: elastic modulus, yield stress and strain hardening
- Boundary conditions: clamped, pinned or free
- Impact velocity: strain rate and inertia effects
- Imperfections: amplitude and shape

The energy absorption efficiency of a structure is evaluated by various indicators such as: peak force, total energy absorption and specific energy absorption. In case of progressive buckling, the total energy absorbed by a structure is dependent on the modes of deformation.

Nomenclature	
b	Width of the square tube
h	Height of the square tube
m, n	Johnson -Cook material constants
t	Thickness of the square tube
$A, B, C,$	Johnson -Cook material constants
TH	Homologous temperature Melting temperature of
Tm	material
T_R	Room temperature
ΔT	Temperature change due to conversion of plastic
Greek Symbols	
β	Factor of conversion for plastic energy to heat
p_{eff}	Effective plastic strain
ε_{Peff}	Effective plastic strain rate
$\dot{\varepsilon}$	Dimensionless plastic strain rate
$\dot{\varepsilon}_0$	Reference strain rate
υ	Poisson's ratio
ρ	Density of the material
σ_{flow}	Flow stress
Abbreviations	
ASTM	American Society for Testing and Materials
EDM	Electrical Discharge Machining

There are four basic modes of deformation in case of axial compression of square tubes: a) Symmetric, b) Asymmetric of Type -1, c) Asymmetric of Type-2 and d) Extensional mode. These modes are dependent on the width to thickness (b/t) ratio. Although symmetric mode occurs for thicker tubes and both asymmetric and extensional mode occurs for thinner tubes, it is dependent on the rate of loading such as quasi-static and dynamic conditions in addition to ratio of (b/t) [4]. The critical length for progressive buckling and global buckling changes according to the loading conditions [5] and is dependent on impact velocity; the critical length of bucking increases with increase in impact velocity. The fold length and crushing distance differ for different modes of deformation. The effective crushing distance plays an important role in the energy absorption which is dependent on the material property and the mode of deformation. Abramowicz [6] proposed a simplified method to calculate the effective crushing distance taking in to consideration the strain hardening response of the material.

In dynamic (progressive) buckling, the strain rate for each fold formation is different as the deformation progresses. This affects the transient strain rate on the fold formation pattern and the crushing force profile, which is directly related to the energy absorption efficiency of the structure; but, this aspect has not been clearly understood. Most of the numerical simulations of high strain rate deformation are carried out using Cowper-Symond equation [7, 8] which takes care of increase in flow stress due to strain hardening. But at high strain rate conditions, due adiabatic condition at deformation, there is a temperature rise due to the conversion of plastic energy to heat which has been studied by Rajeev Kapoor and Nemat-Nesser [9] amongst other researchers.

For a certain mode of buckling, the spike in load value of each fold is closely related to the local flow stress which depends on the local strain, strain rate and temperature. For a material whose flow stress is temperature dependent, continuous rise in temperature during

deformation results in simultaneous lowering of flow stress. The combined effect of strain hardening and thermal softening during high strain rate on fold pattern and energy absorption of thin walled structure is addressed in this paper.

Axial compression of square tubes is conducted at various displacement rates of an axial actuator experimentally. Numerical simulations of the experimental conditions are then conducted by explicit nonlinear finite element code LS- DYNA®. The numerical results including deformation modes and crushing force response are compared with the experimental results. Numerical simulation for different higher strain rates has been performed and their deformation pattern has been analyzed as part of this study.

METHODOLOGY

Material Model

According to Cowper-Symond material model, flow stress is a function of strain rate and it does not include the effect of temperature. In the present work, the von Mises flow stress of the tube material is described using Johnson-cook (Equation 1) [10] constitutive model which takes care of the strain hardening and thermal softening at high strains.

$$\sigma_{flow} = [A + (B\varepsilon_{eff}^{p})^{n}](1 + C \ln \dot{\varepsilon})[1 - (T_{H})^{m}] \tag{1}$$

Where A is the yield stress

B, C, n, m are material constants

ε_{Peff} is the effective plastic strain

$\dot{\varepsilon} = \dot{\varepsilon}^{P}_{eff}/\dot{\varepsilon}_{o}$ is the dimensionless plastic strain rate for a reference strain rate $\dot{\varepsilon}_{o}$ and T_{H} is a form of homologous temperature given as $T_{H} = (T-T_{R})/(T_{m}-T_{R})$. T_{M} is the melting temperature of the material and T_{R} is the room temperature. Values of A, B and n are found at $T_{R} = 28°C$.

The expression in the first set of brackets gives the stress as a function of strain for $\dot{\varepsilon} = 0$ and $T_{H}=0$. The expression in the second and third set of brackets represents the effect of strain rate and temperature respectively.

Tensile Test

Tensile specimen is prepared from one of the sides of the square tube by using Electrical discharge machining (EDM) according to ASTM E-8 standards. Use of EDM ensures dimensional accuracy and avoids the presence of residual stress during specimen cut from thin walled tube of thickness of 1 mm. The dimensions of the specimen are given in Figure 1. The tensile test is conducted at very low displacement rate of 5 mm/min by using a 100kN MTS 810 servo hydraulic machine.
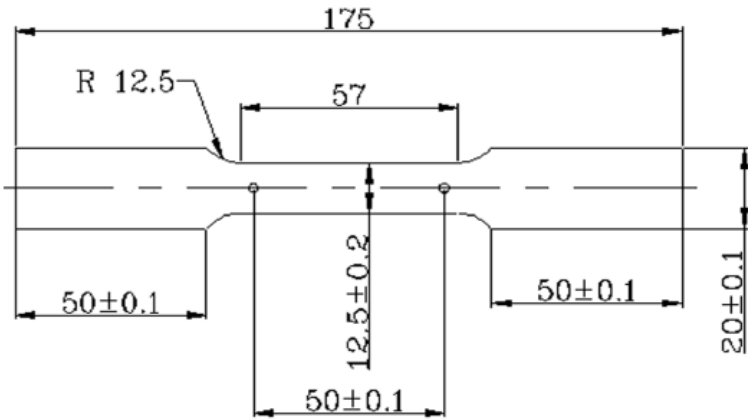
Figure 1. Tensile specimen dimension

The data obtained from the tensile test is used to plot the stress-strain graph (Figure 2). The yield stress A is found from the stress strain graph by drawing a 0.2% strain offset line parallel to the initial stress-strain slope of the curve . The Johnson-cook material parameters B and n are found by using the curve fitting of the plastic part of the true stress-strain curve. The material constants are found from the stress strain curve (Table 1) which is used in the numerical simulation.

Table 1. Material constants obtained from tensile test

Material Constants	Values
Young's Modulus (GPa)	69.6
Yield stress (MPa)	172.8
A (MPa)	172.8
B(MPa)	431.09
N	0.650
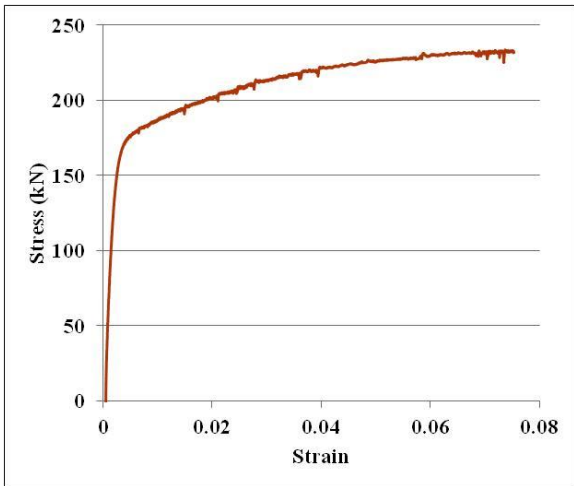
Figure 2. True stress-strain curve of extruded tube from tensile test.

Experimental Details

Thin walled Aluminium square tubes of size 150 mm (h) x 25.4 mm (b) x 1 mm (t) are axially compressed in an MTS 810 servo hydraulic machine equipped with computer control and data acquisition system at various actuator displacement rates of 1000 mm/min, 2000 mm/min and 3000 mm/min. The testing is done under displacement control with the bottom platen of the test system being moved vertically upward to compress the specimens up to a distance of 50 mm. The sides of the specimen are marked with a 5 mm x 5 mm grid for measuring the deformation. A Micro-epsilon Infrared thermal imaging camera (TIM-160) is used to observe the rise in surface temperature of the focal side during axial compression of the square tube due to large plastic deformation. The experimental set up is shown in Figure 3.
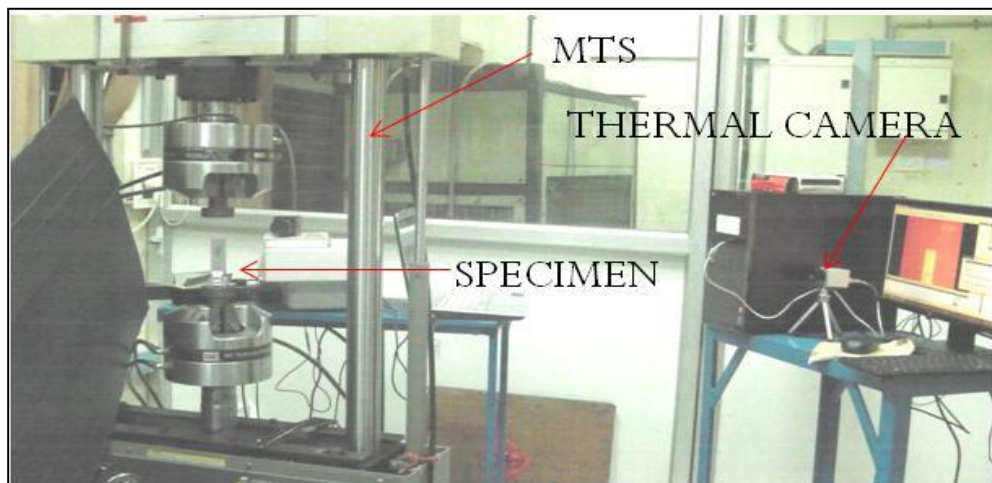

Figure 3. Test setup

Parametric Study

Laboratory tests are quite time consuming and expensive. So it is therefore desirable to carry out the numerical study of compression behaviour to understand the deformation behaviour of square tubes at high strain rates. The analyses are carried out for different velocities ranging from 3 m/s to 14 m/s.

RESULTS AND DISCUSSION

The load-displacement curve obtained at different displacement rates is shown in Figure 4. It is noted that there is a peak force after initial elastic loading and there is collapse of load after some displacement, representing specimen folding. Thereafter, the load increases as the specimen fold during dynamic buckling is complete. This process repeats for each fold formation. It is noted that the peak force decreases with subsequent fold formation in this material. We can observe that the peak force and the overall crushing force profile increases with increasing the strain rate from 1000 mm/min to 3000 mm/min. The change can be due to strain hardening. The difference in the curve pattern of load-displacement response at two deformation rates can be due to the shifting of fold length with strain rate or due to some minor imperfections during manufacturing process.

Deformation Mode

Symmetric deformation mode of deformation is observed which can be predicted for the particular b/t ratio [4] in quasi-static condition and the same is shown in Figure 5.
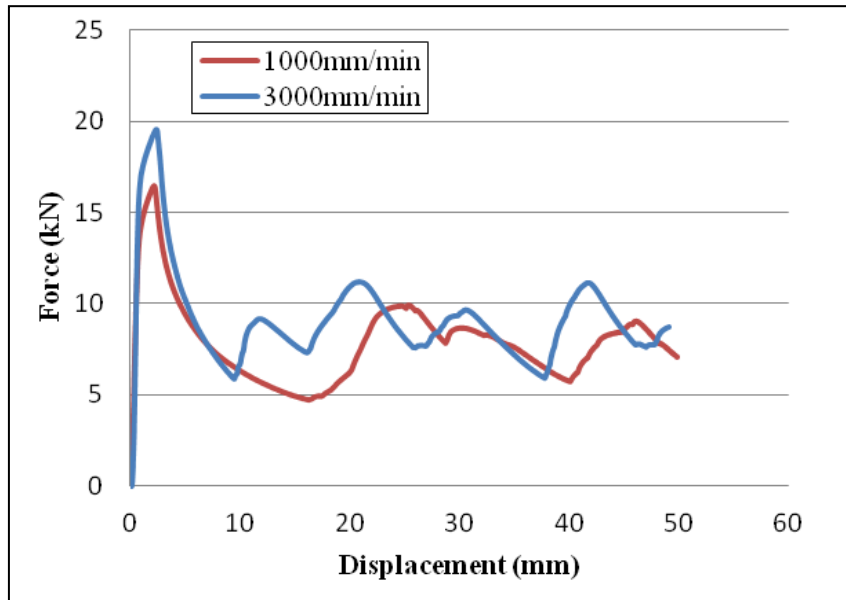

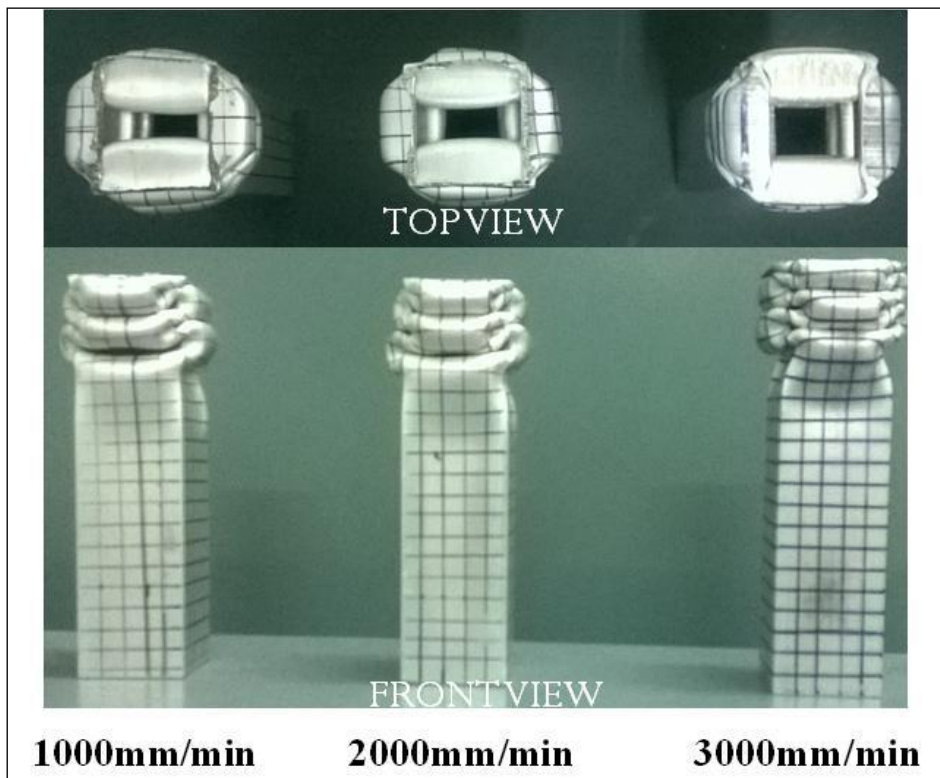**Figure 4.** Force-displacement curve for different strain rates

Figure 5. Deformation mode for quasi-static axial compression

Thermo-Graphy Results

In case of high strain rate loading, where the process is adiabatic, one could expect 100% of conversion of plastic energy to heat which is given by the following equation [8].

$$\Delta T = \beta \frac{1}{\rho C_p} \int \sigma d\varepsilon_{eff}^{p} \qquad (2)$$

Where ρ is the mass density, Cp is the specific heat and β is the factor of conversion for plastic energy to heat. The value of β is 1 in the case of a 100% adiabatic process.

During axial compression at different deformation rates, as in the present study, the overall rise in the temperature is observed to be around 20°C and the same is shown in Figure 6. The amount of temperature rise might not seem very significant in case of quasi-static loading where the conversion of plastic energy to heat is not completely adiabatic. Further, this temperature rise is measured as radiation component from the specimen across a selected window, which is much larger in size compared to local heating region at the fold of the specimen. Other heat transfer mechanisms such as conduction and convection could have also resulted in heat loss from the specimen.

Numerical Analysis

Numerical simulation of compression response of tubular member is performed using LS-DYNA® explicit solver. The finite element model of the tube is constructed with four node Belytschko shell element. *MAT-JOHNSON-COOK TITLE is used to define the material model of the tube. *CONTACT-AUTOMATIC-SINGLE- SURFACE is defined for the tube with its walls. Compression load is given through a *PLANAR MOVING RIGID WALL. *CONTROL-HOURGLASS is activated in order to control the zero-energy modes of deformation.
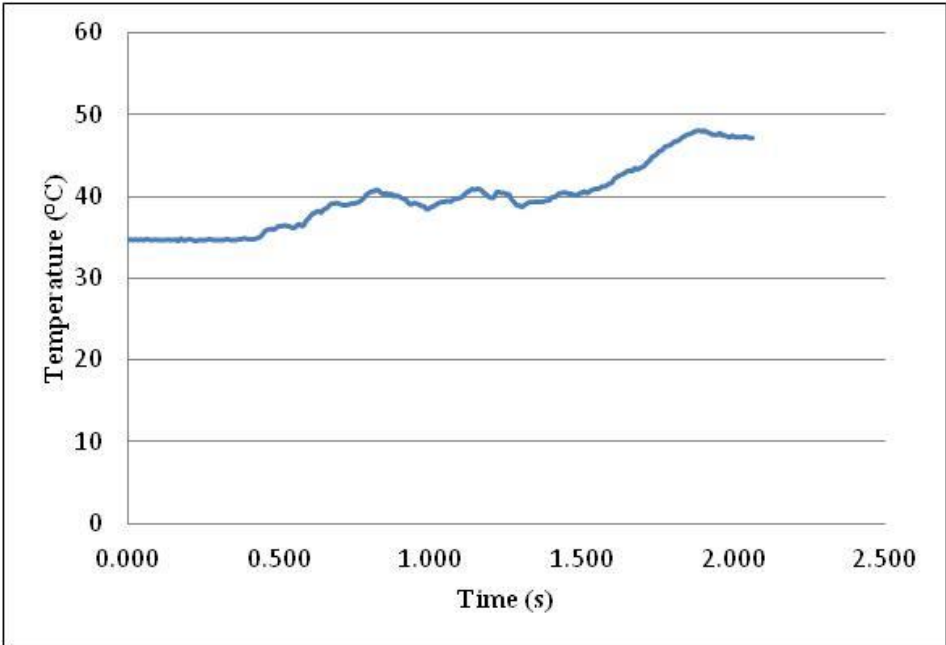
Figure 6. Surface temperature variation during axial compression at strain rate 3000 mm/min

Johnson-Cook material constants A, B and n are taken from the tensile test (Table 1). The material parameters for hollow extruded tubes are quite different than solid bars of the same material. The values of these parameters normally found by experimental methods like Split Hopkinson pressure bar testing; data obtained from solid bars cannot be used for in the case of hollow tubes as the deformation modes are different. Hopkinson's bar data cannot be accurately evaluated after necking starts in the tensile specimen. Furthermore, at large stain rates adiabatic heating complicates the results. In view of this, initial trial values of C and m are taken from the literature [11] given for the aluminium alloy. Through inverse modelling approach, the values of C and m are found to be 0.0083 and 1 respectively (empirically) by trying to match the results of numerical prediction with the experimental results. Other material constants used in the numerical simulation are given below in Table 2.

Table 2. Material constants used for numerical simulation

| Material constants	Value
Density (Kg/m^3)	2700
Shear modulus (GPa)	27
v	0.3
Specific Heat(Cp) (J/Kg-°C)	875
T_m (°C)	650

Validation of Numerical Model

The numerical model is validated for the strain rate of 3000 mm/min. The model is validated by three criteria: a) match the folding pattern, b) force-displacement curve and c) change in total internal energy in the tube during compression. The comparison of the folding patterns between the experiments and numerical simulation is shown in Figure 7. The force displacement profile for numerical and experiment curve have a similar pattern but the overall numerical force values are little lower than the experimental values (Figure 8) except for 1st peak force. As a consequence, the total internal energy absorption of the numerical model is slightly lower than the experimental result (Figure 9). Also it is to be noted that there is hourglass energy in case of numerical simulation which are defined as zero energy modes of deformation that produce zero strain and no stress. The hourglass energy in the numerical simulations is less than 5% of the total energy according to the numerical standards.
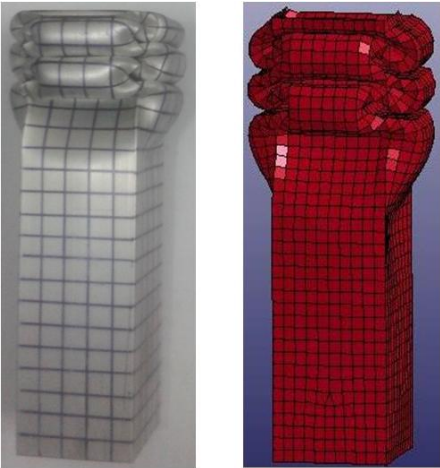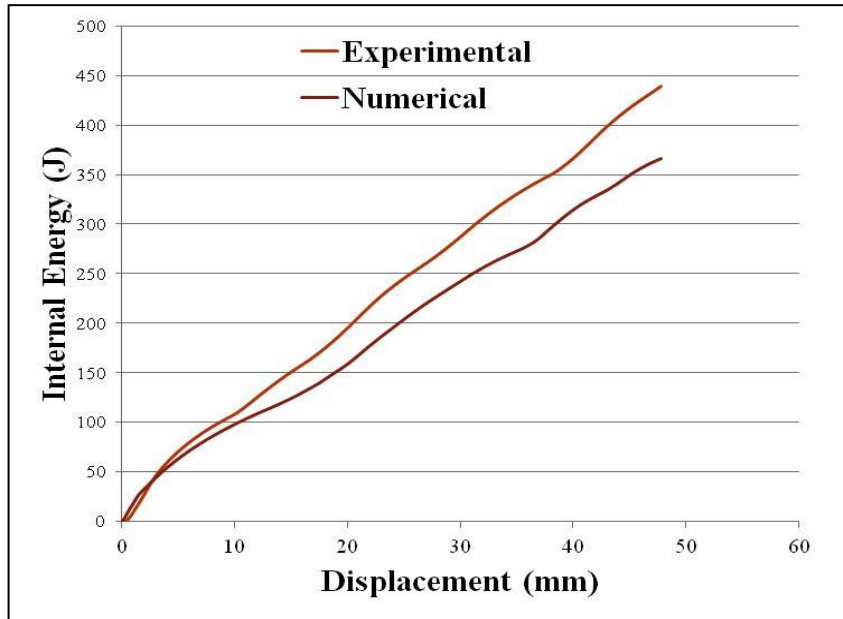
Figure 7. Deformation pattern after compression
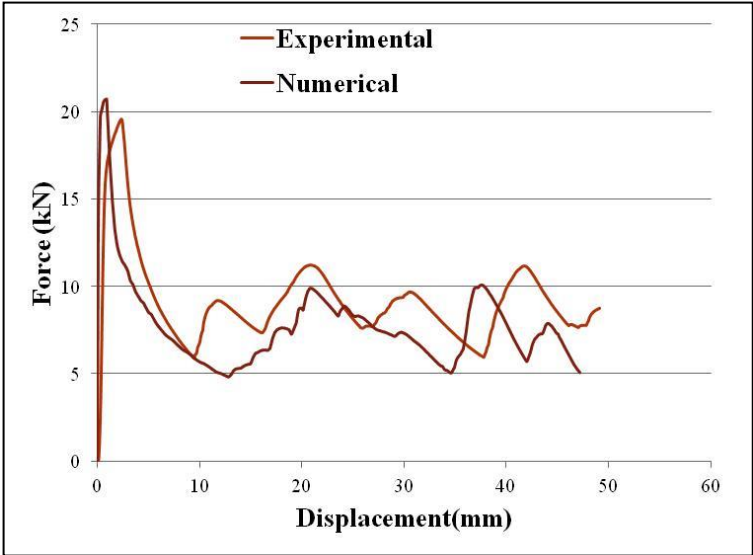
**Figure 8.** Force-displacement curve for experimental and numerical simulation

Figure 9. Internal Energy -displacement curve for experimental and numerical simulation

Results of Parametric Study

Symmetric, asymmetric type1 and type 2 and extensional modes and mixed modes are observed for different strain rates. Symmetric mode dominates in lower strain rates (velocities of 3 to 5 m/s). Scaling laws for dynamic buckling are implemented according to Ref. 12 for the numerical simulation for higher strain rates.

The peak forces for various strain rates are plotted in Figure 10. The peak forces increases with increasing impact velocity which is due to the effect of strain hardening at higher strain rates. The rates of increase of peak force are different for different ranges of impact velocity.
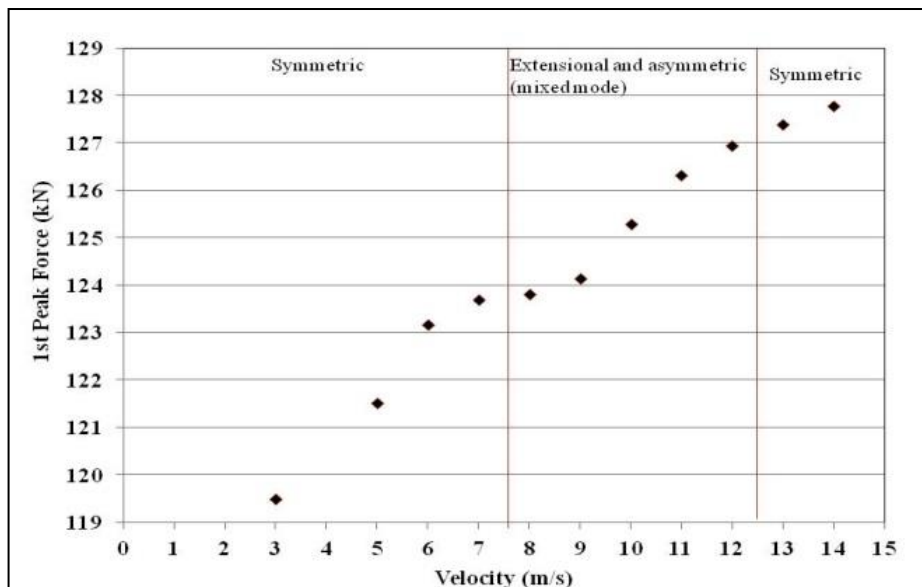
Figure 10. Variation of peak force during dynamic buckling for different strain rates

The total energy for various strain rates are plotted in Figure 11. The energy absorption is more for the velocities where extensional and asymmetric mixed modes are observed.

Validation of numerical model of Aluminium square tube is done for quasi-static loading conditions. After the first fold, the pattern and peak force decreases subsequently due to the temperature parameter 'm' whose effect is more significant at higher strain rates. Simultaneously, the effect of strain rate hardening parameter C is reduced as the strain rate decreases with subsequent fold formation. The mismatch in the numerical and experimental results can also be due to the assumption that the tube is isotropic. The tube material may not be homogenous due to the imperfections during the manufacturing process.
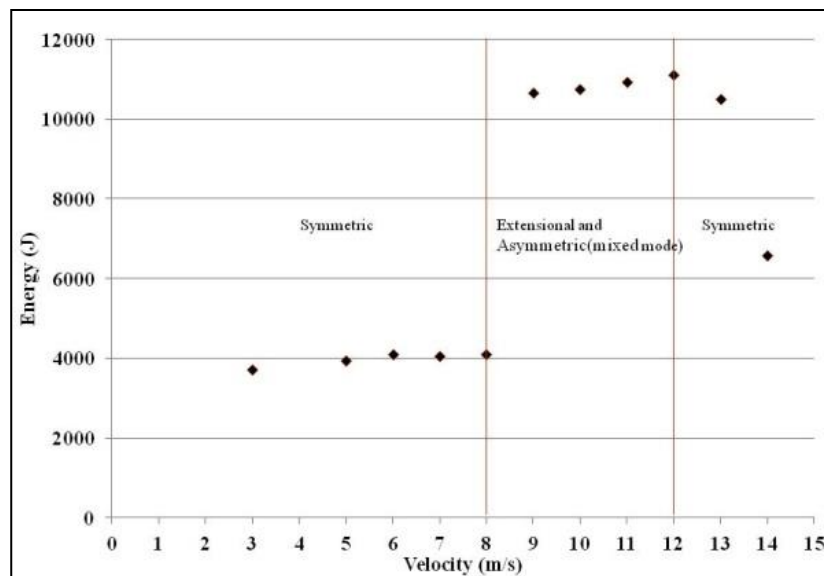

Figure 11. Variation of total energy for different strain rates

CONCLUSION

The parametric study for higher strain rates are performed by the validated numerical model.
- Different modes of deformation patterns are found for different strain rates
- The lowering of internal energy after a certain velocity can be due to thermal softening

Further study is required for better understanding of deformation pattern at higher strain rates.

REFERENCES

[1] Wierzbicki, T. and Abramowicz, W., (1983). On the crushing mechanics of thin-walled structures. *Journal of Applied mechanics*, **50**(4a): 727-734.

[2] Abramowicz, W. and Jones, N., (1986). Dynamic progressive buckling of circular and square tubes. *International Journal of Impact Engineering*, **4**(4): 243-270.

[3] Alghamdi, A.A.A., (2001). Collapsible impact energy absorbers: an overview. *Thin-walled structures*, **39**(2): 189-213.

[4] Langseth, M. and Hopperstad, O.S., (1996). Static and dynamic axial crushing of square thin-walled aluminium extrusions. *International Journal of Impact Engineering*, **18**(7-8): 949-968.

[5] Karagiozova, D., Alves, M. and Jones, N., (2000). Inertia effects in axisymmetrically deformed cylindrical shells under axial impact. *International Journal of Impact Engineering*, **24**(10): 1083-1115.

[6] Abramowicz, W., (1983). The effective crushing distance in axially compressed thin-walled metal columns. *International Journal of Impact Engineering*, **1**(3): 309-317.

[7] Abramowicz, W. and Jones, N., (1984). Dynamic axial crushing of square tubes. *International Journal of Impact Engineering*, **2**(2): 179-208.

[8] Jones, N., (1989). Recent studies on the dynamic plastic behavior of structures. *Applied Mechanics Reviews*, **42**(4): 95-115.

[9] Kapoor, R. and Nemat-Nasser, S., (1998). Determination of temperature rise during high strain rate deformation. *Mechanics of Materials*, **27**(1): 1-12.

[10] Johnson, G.R. and Cook, W.H., (1985). Fracture characteristics of three metals subjected to various strains, strain rates, temperatures and pressures. *Engineering fracture mechanics*, **21**(1): 31-48.

[11] Johnson, G.R. and Cook, W.H., (1983), April. A constitutive model and data for metals subjected to large strains, high strain rates and high temperatures. In *Proceedings of the 7th International Symposium on Ballistics,* 21: 541-547.

[12] Jones, N., (2011). *Structural impact*. Cambridge university press.

[13] LS DYNA® Theory manual, (2006). *User's Manual*.

Sampling Strategy for Flatness Tolerance Evaluation by Coordinate Measuring Machine

Siriluk Phankhoksoong[1], Anchasa Pramuanjaroenkij[2], Chatchapol Chungchoo[2]
[1]Department of Mechanical Engineering, Kasetsart University, 50 Nyam Wong Wan Rd., Lat Yao, Chatuchak, Bangkok 10900, Thailand.
[2]Department of Mechanical and Manufacturing Engineering, Kasetsart University, Chalermphrakiat Sakon Nakhon Province Campus, Sakon Nakhon 47000, Thailand
(*corresponding Author: fengcpc@ku.ac.th)

Abstract   In geometrical tolerance investigations, the measurement accuracy plays an important role for measured samples to be based on standard codes while measurement procedures must meet the code requirements. This work introduced the number of sampling point strategy for the high accuracy by using coordinate measuring machine (CMM) to measure the flatness tolerance of the specimen. This specimen was prepared by CNC milling and followed ISO 10791-7-A160 standard. Firstly, the surface deviation was measured using Ballbar diagnostics to find the number of vibration waves. Then, this number was used to specify the number of measured flatness tolerance points on the surface which was gridded by Polar grid extraction strategy. The flatness tolerance results obtained by the number of sampling point strategies with counting the wave number were compared with the results obtained from the traditional method. The strategies showed its potential in estimating the number of measured points on any standard disc surfaces to find their flatness deviations.

INTRODUCTION

Measurement is the process of experimentally obtaining information on the magnitude of a quantity and involves a measurement procedure that relies on theoretical model. Before any measurement can be conducted, a calibrated measuring system is required and may be confirmed later in the design of precision machine tools or mechanisms to be established to define the accuracy. There are detailed descriptions in the product which is produced or manufactured by the machine tool or by the assessment of the tasks performed by the mechanical system according to the specifications [1].

Current competitive products rely on high-precision manufacturing processes, machines, and control technologies. To control the product quality and reliability, its quality is determined to meet the standards in the manufacturing processes. Geometric Dimensioning and Tolerancing (GD&T) consists of all symbols, definitions, mathematical formulae, and application rules and represents both the nominal dimensions (ideal geometry), and the tolerances for parts. Codes or standard codes, which refer to the flatness in the form of the tolerance, are ANSI/ASME Y14.5M-2009 and ISO/TS 12781-2. Inspection of flatness is usually based on a cloud of points that must be measured on the machined surface. The Coordinate Measuring Machine (CMMs) provides the most common accuracy

and flexibility among the measurement machines; for example, the 3D surface flatness errors measured by the CMM have differently dimensional metrologies, but their lateral resolution levels are still the same. Furthermore, the flatness error is affected by the processing method and associative method used [2]. The analysis of machining steps of the shape surface could minimize the flatness deviation [3].

With a limited number of flatness tolerance investigations, several algorithms have been investigated and implemented for the tolerance evaluations [4] and one of them is least squares method (LSM). LSM minimizes the sum of squared errors and is the association criterion that is one of the most widely embedded methods in CMM software. The number of points, which will be sampled, plays an important role on CMMs because inappropriately distributed points may provide unreliable references in the results, namely, the greater the number of appropriately distributed measured points is, the more reliable the assessment is likely. The larger number of the contact points consumed a longer time is needed to measure a feature [5]. Raghunandan and P. Venkateswara [6] analysed the sampling strategies, such as the number of section points required for the given surface quality and a statistical analysis of a set of machined features in the sampling strategy design [7]. An alternative technique was devised to arrive at the reduced sampling size by using the large sampling data inspected on the first component as the basis [8].

Normally, the number of measured points relates to the requirements of the same configurations formed by the standard codes. The sample measurements sometimes involve with the performance of each machine used in each manufacture since the machine lifetime affects the machine performance.

This study focused on introducing a new strategy to determine the suitable sampling strategies for estimating flatness deviation on surface workpieces. Regarding number points on a specimen in the flatness tolerance investigation by CMM. The method was derived by results from "accuracy measurement" of a ball-bar tested. CNC milling machine movements was used to specify measuring points and capability of the machine.

METHODOLOGY

THEORETICAL METHOD

Flatness Verification Problem

Flatness tolerance is defined as the zone between two parallel planes where a surface must lie and this tolerance is defined in the main international standards, including ISO 1101, ISO/TS 12781-1 and ASME Y14.5. The flatness error of a measured surface is estimated as the distance between two parallel planes that are set to contain all measured points as shown in Figure 1. According to ISO standards, the LSM can be used to estimate the flatness error, which is the most popular and widely used implementation in most CMMs [9].
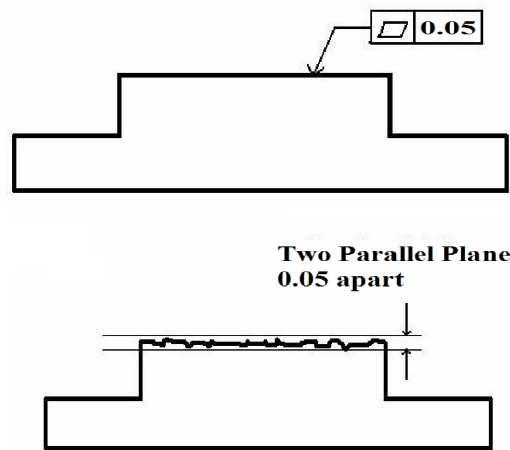
Figure 1. Definition of the flatness tolerance applied on a planar surface [10]

Flatness Measurement based on Least Squares Method (LSM)

According to the GPS (geometrical product specification standards) chain [11], the least squares method used in the flatness measurement is composed of separating, extracting, fitting and appraising components. So, the least-square plane is calculated from data measured and is considered as the ideal surface. The equation of the least-square plane is supposed as follows:

$$z = ax + by + c \qquad (1)$$

where *a*, *b* and *c* are the parameters of the least-square plane [12]. If the coordinate of a workpiece is measured by portable CMM and signed as (x, y, z), i is from 1 to n, in which n is the number of location points, then the distance from every spot to the least-square plane is

$$d_i = \frac{z_i - ax_i - by_i - c}{\sqrt{a^2 + b^2 + 1}} \qquad (2)$$

So, the least-square surface must be guaranteed that the squared summation of all distances is minimal, or

$$D = \sum_{i=1}^{k} d^2{}_i = l \sum_{i=1}^{n} \frac{\left(z_i - ax_i - by_i - c\right)^2}{a^2 + b^2 + 1} = \min \qquad (3)$$

The extreme conditions satisfying equation (3) must be

$$\frac{\partial D}{\partial a} = 0, = \frac{\partial D}{\partial b} = 0, = \frac{\partial D}{\partial c} = 0 \qquad (4)$$

Appropriate Extraction Strategy

For a reliable evaluation of a flat surface, an appropriate extraction strategy must be adopted in order to obtain a representative set of points of workpieces to ensure the reliability of this evaluation. According to ISO 12781-2, the minimum theoretical density of the points, which is necessary to make a flat surface coverage, depends on the harmonic representation.

Practically, it is unrealistic to proceed to the exhaustive coverage of the element flatness, which is defined from this theoretical minimum density of points, in an acceptable time interval by using current technologies. More limited extraction strategies are used in these mentioned situations to provide more specific information as shown in Figure 2. Normally, for a disk configuration, the polar grid extraction strategy was recommended as the sampling strategy for the assessment. The main characteristic of the polar grid extraction is a high density of points along both the radial and roundness profiles. It gives the extraction strategy the ability to assess the harmonic content in both the radial and circumferential directions relative to the form content [13].
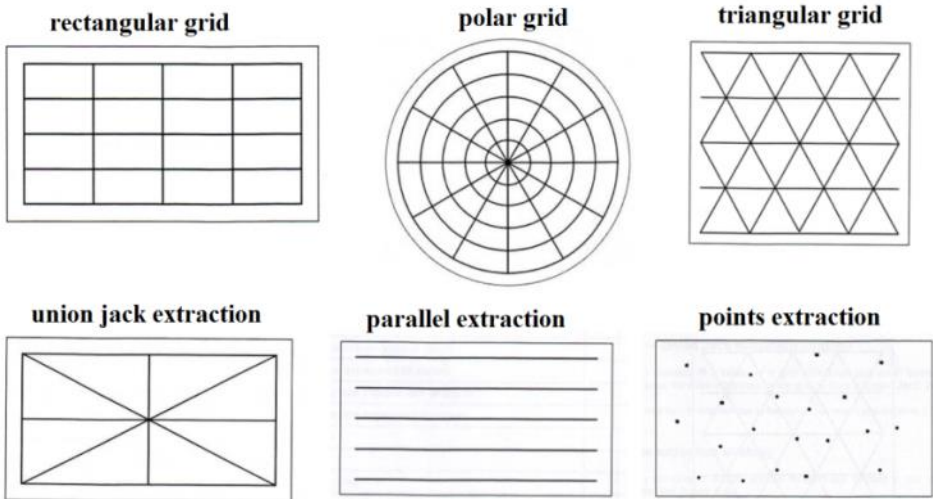
**Figure 2.** Extraction strategies for flatness deviation evaluations [13]

Probing Strategies

A machined workpiece usually combines standard geometric features that can be assigned by the fitting of substitute elements to a number of the measured points. For the measurement purposes, there is the mathematically defined minimum numbers of contact points (Figure 3 and Table 1) that must be used when fitting an element to a geometric feature. For practical purposes, CMM usually operates to measure the workpiece more than this minimum number of points so that any geometric errors in the surface can be determined as shown in Table 1. It is recommended that equally spaced points are not used however, extreme distributions are not recommended [14].

Table 1. Number Of Contact Points Required For Various Geometric Features [14]

Geometrical Feature	Mathematical Minimum	Recommended Number of Sampling Points
Straight line	2	5
Plane	3	9 (approximately three lines)
Circle	3	7 (detect up to six lobes)
Sphere	4	9 (approximately three circles in three parallel planes)
Cone	6	12 (circles in four parallel planes for straightness information)
		15 (five points on each circle for roundness information)
Ellipse	4	12
Cylinder	5	12 (circles in four parallel planes for straightness information)
		15 (five points on each circle for roundness information)
Cube	6	18 (at least three per face)

To achieve a nearly uniform distribution of (N) points on a plane, it should be divided into a N1×N2 sub-table where N1×N2 is approximately equal to N. A suitable pattern can be achieved by selecting a random position for each individual point. The points on the lines are selected according to the procedure detailed above for the line measurement [14]. Table 1 is an extract from BS7172: 1989 and recommends the minimum number of points per feature.
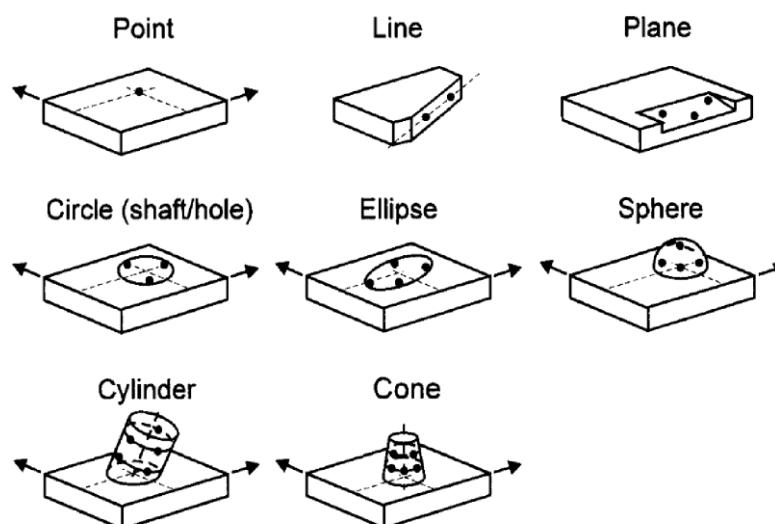
Figure 3. Defining common geometric features [14]

Figure 4 shows the spacing effect, c, of the assessed points on the surface exhibiting sinusoidal form deviations of the wavelength λ [15]. When the spacing c is greater than half of the wavelength, λ, the wavelength of the sine wave cannot be assessed as shown in Figure 4 (a). When the spacing is 0.4 λ, the wavelength of the sine wave will be assessed; however, some amplitude will be considerably reduced as shown in Figure 4 (b). When the spacing c, is equal to 0.2 λ, the true shape of the sine wave (wavelength and amplitude) is almost obtained as shown in Figure 4 (c). This technique could lead to very time-consuming and costly inspections because of its complication. Therefore, the number of selected sections and the number of probed points are normally reduced, but these numbers should be distributed in an optimized way, which depends on the type (shape) of the form deviation of the manufacturing process, the magnitude of form deviation, ratio of form deviation to the geometric tolerance, and the geometrical characteristic to be assessed.


(a)

(b)

(c)
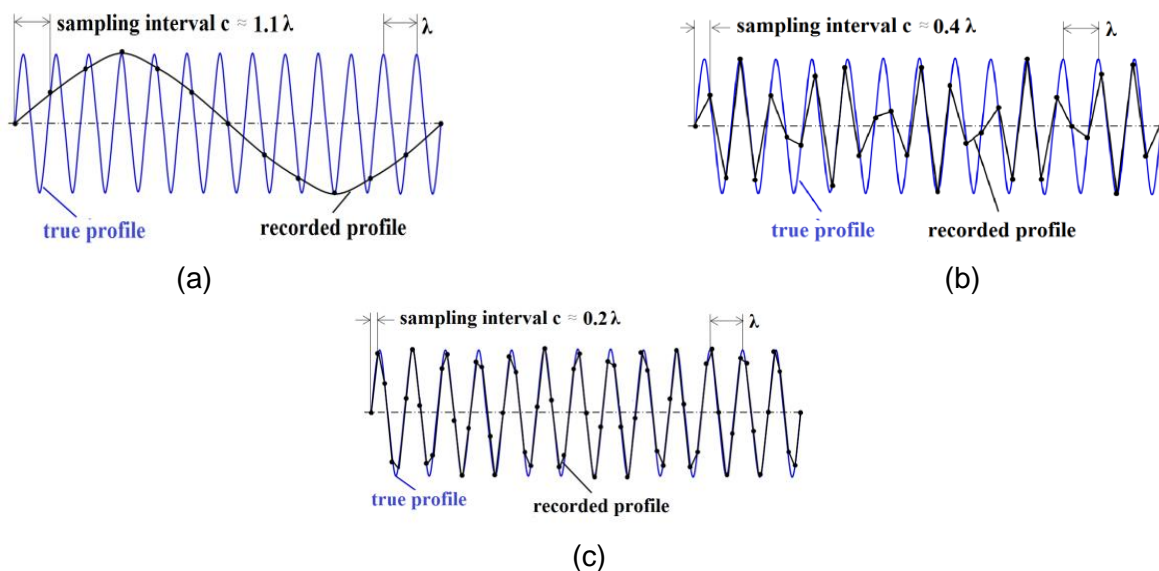
Figure 4. Assessment of sinusoidal form deviations depending on the spacing of assessed points relative to the wavelength of the sine wave [15]
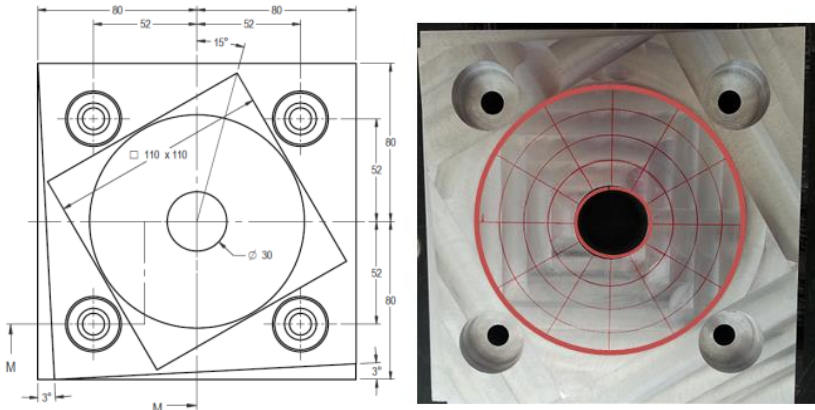
Sampling Strategy
The main objective of this work was to focus on a new strategy to determine the suitable sampling strategies for the accurate evaluation number of point flatness error on surface workpieces using the CMM. This approach applied the LSM method for flatness error estimation, the polar grid extraction strategy as the reliable evaluation of a flat surface, and a special search technique to arrive at the number of sampling points based on surface error values obtained from Ballbar diagnostics size. The experimental method involved the following stages: (a) machining the sample parts and measuring the test pieces; (b) applying the sampling strategy to obtain the number of point sample size; and (c) evaluating the specimen accuracy.

Text Font of Entire Machining of Parts and Measurement of Test Pieces
In order to verify the new concept introduced in this paper, AA-5083 aluminium test pieces (according to ISO 10791-7-A160 [16]) were cut at three positions by CNC machine, Chevalier 2040 VMC (Figure 5). At each position, the geometric errors in the machine tool were assessed by Renishaw QC10 ball-bar. For each test piece as shown in Figure 6, the CMM inspection was performed by a touch-trigger probe, which was probed on the disc surfaces and their locations were recorded, and the dimensions were recorded in parts that could be calculated. The computer software (PowerINSPECT 2013) maintaining a database of qualified stylus was used in an inspection report.
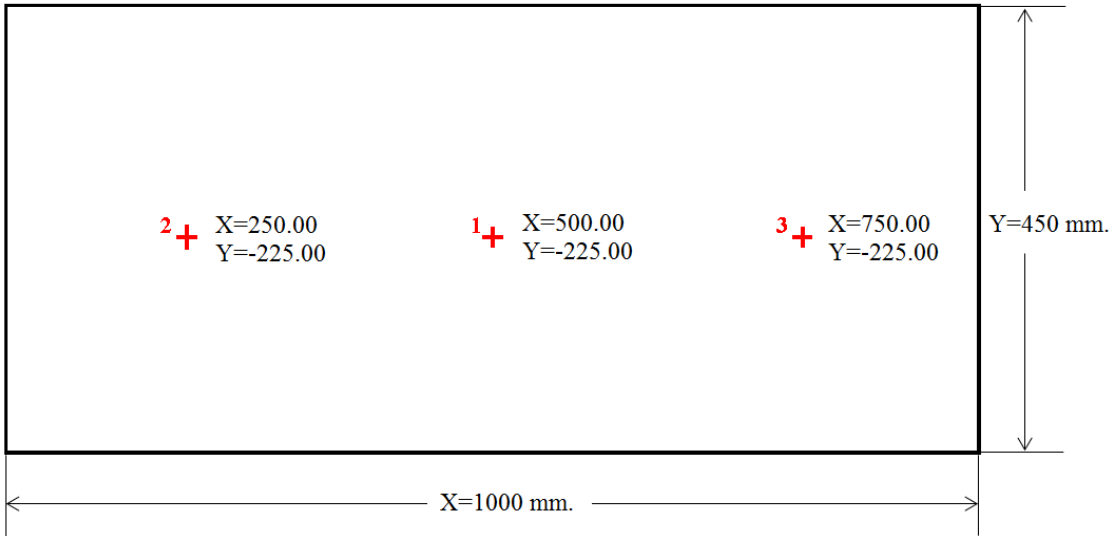
Figure 5. Three cutting positions on the table

Figure 6. Top view of the small-size contouring of the test piece with ISO 10791-7

Sampling Strategy for the Number of Point Sample Sizes
For example Figure 7-8 shown geometric errors of machine tools at position 1 (at the centre of the machine table) and the errors on the Z axis could be observed. The highest error value was selected and then the number of waves was counted in the circular motion on the ZX plane around 360 degrees (Figure 7) and on the YZ plane around 360 degrees (Figure 8)

at position 1. Later, the number of waves was calculated by crossing both planes that are shown at equations (5). Employing the proposed method mentioned earlier, the number of points was about 240.

$$N = \frac{N_x}{2} \times \frac{N_y}{2} \tag{5}$$

Where N is the population size, N_x is number of waves was counted in the circular motion on the ZX plane around 360 degrees and N_y is number of waves counted in the circular motion on the YZ plane around 360 degrees.
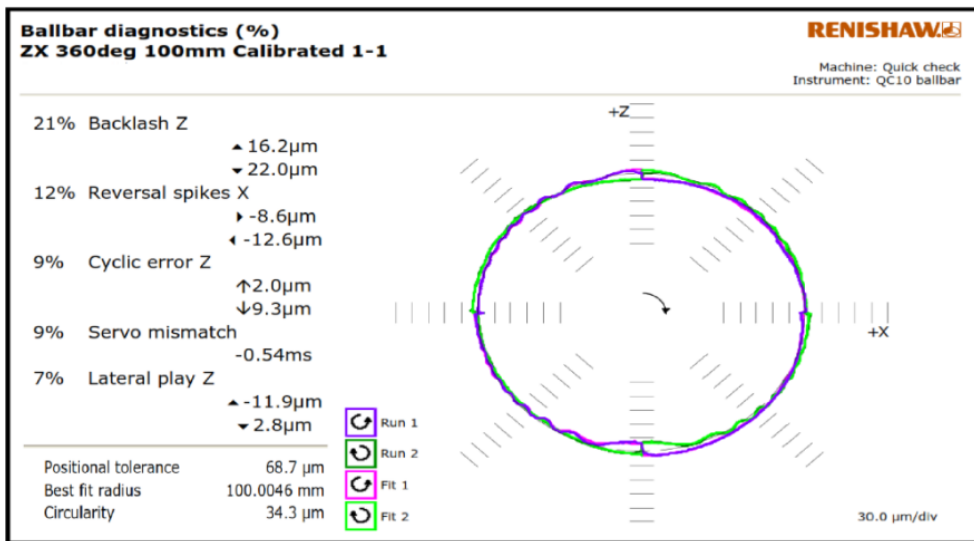

Figure 7. Machine tool calibration at position 1 measured by ball-bar diagnostics on the *ZX* plane around 360 degrees
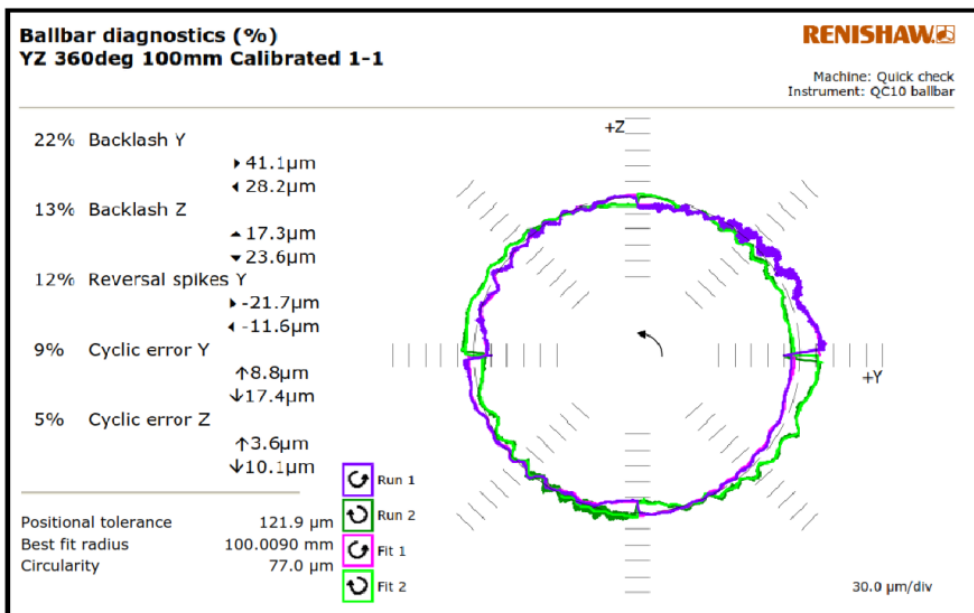

Figure 8. Machine tool calibration at position 1 measured by ball-bar diagnostics on the YZ plane around 360 degrees Statistical sampling strategies by CMM

The sample used in this research was prepared by a staff based on the sample size sitting at a 95% confidence level of errors or not exceeding 5% precision level by using the ratio formula to determine the sample size [17]. The following equations can be solved to obtain *n*, *N*, and *e*, where n is the sample size, *N* is the population size and *e* is the precision level.

$$n = \frac{N}{1 + Ne^2} \qquad (6)$$

We obtained the 95 % confidence level of errors at $n = \dfrac{240}{1 + 240(0.05)^2} \approx 150$; and 90%

confidence level of errors at $n = \dfrac{240}{1 + 240(0.10)^2} \approx 72$

To experiment the efficiency of sampling relevant to the CMM probe path, Figure 9 shows the positions of the points probing by the CMM chosen by the different signature-based polar grid extraction strategy that was recommended as the sampling strategy for the assessment of the total feature of flatness that is nominally a disk.
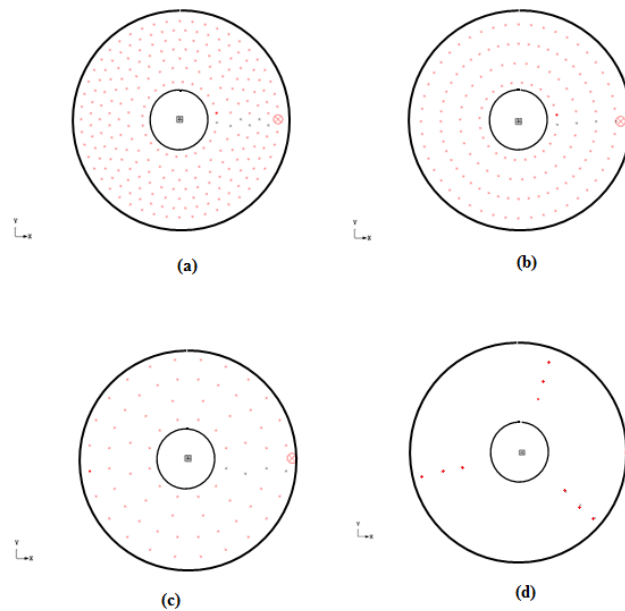
Figure 9. Coordinates of each sampling strategy. Wave number on the XZ plane crossing the YZ plane is equal to 240 points; (b) 150 points were sampled 95% interval confidence of (a); (c) 72 points were sampled 90% interval confidence of (a); and (d) 9 points were recommended number of standards

Accuracy of the flatness error data from the new strategy was obtained by using the CMM on 3 positions of the CNC milling table and measured 3 times on the disc surface workpieces. The measurement for each case was recorded and the discrepancy rate was calculated based on the maximum achievable accuracy of the measurement. The average discrepancy rate (*r*) was computed [18] from;

$$r = \frac{(a-b)}{a} \times 100 \qquad\qquad (7)$$

where a is a value considered as the highest achievable accuracy for the disc surface workpiece and b is the mean (Avg.) data value obtained through the experiment for the number of the point sampling size.

RESULTS AND DISCUSSION

When the sampling points were maintained at the high level of quality, it has been shown that the accuracy could be observed. Figure 10 shows four measuring strategies compared for indicates the accuracy of the flatness error results from the new strategy. Statistically analysing the data obtained through the experiments, the new sampling strategy had a significant effect on the accuracy of the flatness of the disc surface. Positions 1 and 2, at 150 points (95% points of the sampling) and 72 points (90% points of the sampling), were not significantly different (around 5% interval confidences) while the flatness on position 3 provided the close results shown Figure 11. In order to increase the reliability of the measuring geometric errors of the workpiece, the appropriate number of the sampling points was needed to be employed. In this research, it was found that this number should be more than 90% of the sampling points by calculating cycle wave on the surface profile.
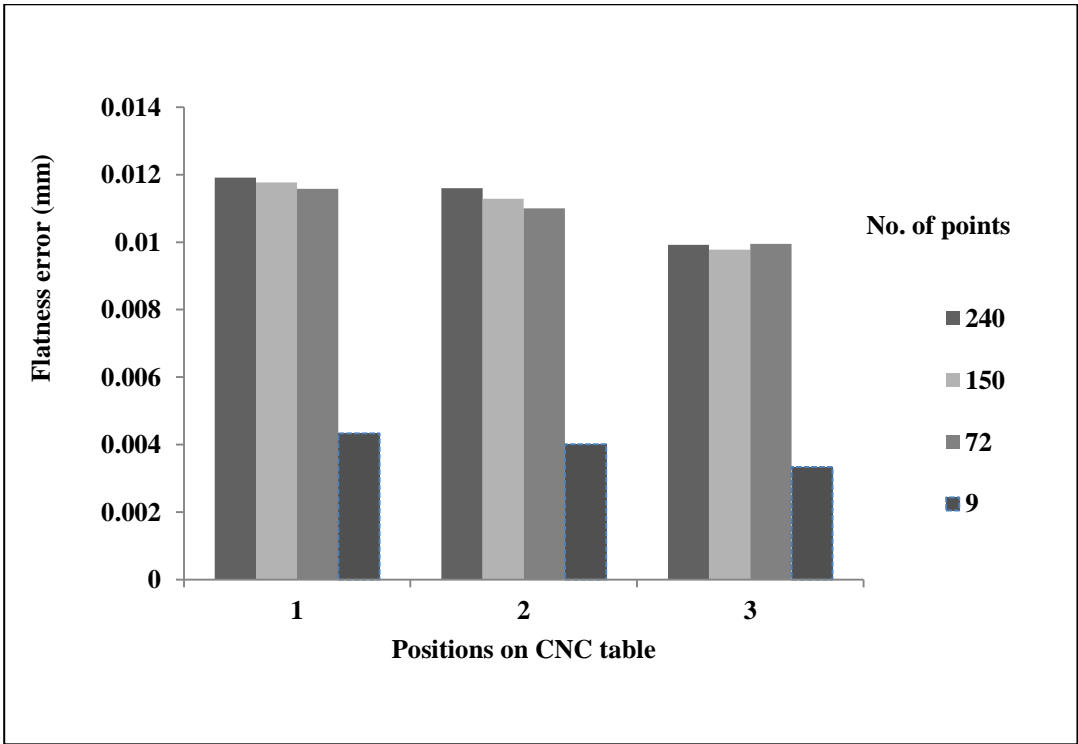

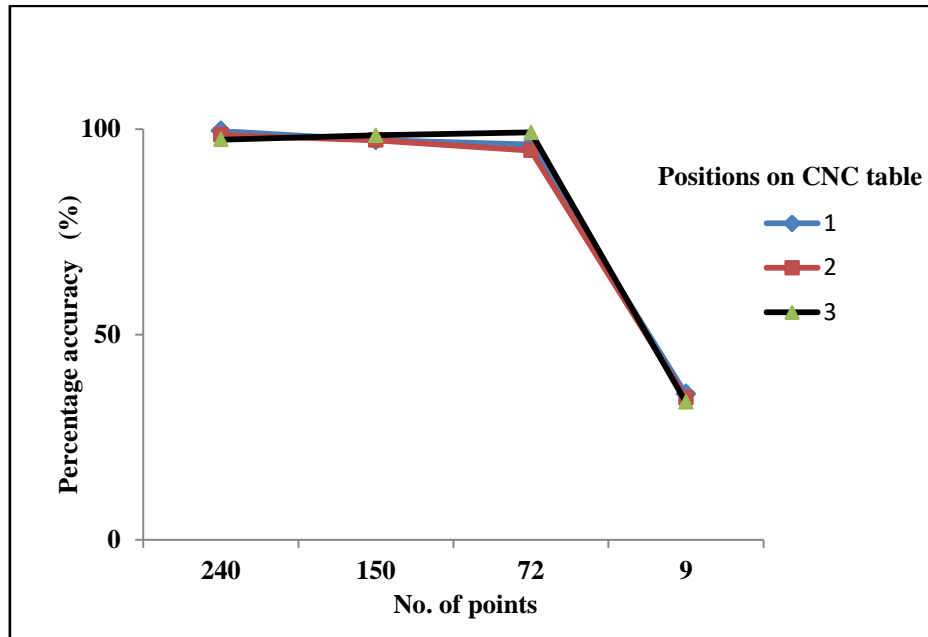**Figure 10.** Flatness error results from the new strategy

Figure 11. Percentage accuracy of flatness error results from the new strategy

CONCLUSION

In this paper, the sampling strategy was presented to implement flatness tolerance evaluation applying the least square method (LSM) from CMM data. The initial population generating the sampling number of the points was given from the wave numbers of ballbar diagnostics from CNC milling machine results. Comparing between new strategies with conventional evaluation methods, the proposed strategy revealed the advantages of its algorithm simplicity and good flexibility. The flatness error estimation could be achieved at sufficiently reduced sample sizes with a good degree of accuracy (90% and above), ensuring that the measurement was consistent with the guidelines laid down in the standards for flatness error inspection and the results also confirmed that the proposed method could search the optimal solution efficiently and it was well suited for errors from evaluation of the CMMs.

ACKNOWLEDGMENTS

REFERENCES

[1] Mekid, S. (2008). *Introduction to precision machine design and error assessment*. Taylor & Francis Group.

[2] Hadžistević, M., Štrbac, B., Spasić Jokić, V., Delić, M., Sekulić, M. and Hodolič, J., (2015). Factors of estimating flatness error as a surface requirement of exploitation. *Metalurgija*, 54(1): 239-242.

[3] Nadolny, K. and Kapłonek, W., (2014). Analysis of flatness deviations for austenitic stainless steel workpieces after efficient surface machining. *Measurement science review*, 14(4): 204-212.

[4] Tseng, H.Y., (2006). A genetic algorithm for assessing flatness in automated manufacturing systems. *Journal of Intelligent Manufacturing*, 17(3): 301-306.

[5] Huang, J., (2003). An efficient approach for solving the straightness and the flatness problems at large number of data points. *Computer-Aided Design*, 35(1): 15-25.

[6] Raghunandan, R. and Rao, P.V., (2008). Selection of sampling points for accurate evaluation of flatness error using coordinate measuring machine. *Journal of Materials Processing Technology*, 202(1): 240-245.

[7] Colosimo, B.M., Moya, E.G., Moroni, G. and Petro, S., (2008). Statistical sampling strategies for geometric tolerance inspection by CMM. *Economic Quality Control*, 23(1): 109-121.

[8] Raghunandan, R. and Rao, P.V., (2007). Selection of an optimum sample size for flatness error estimation while using coordinate measuring machine. *International Journal of Machine Tools and Manufacture*, 47(3): 477-482.

[9] Vicario, G., Ruffa, S., Panciani, G.D. and Ricci, F., (2010). Form tolerance verification using the Kriging method. *Statistica Applicata-Italian Journal of Applied Statistics*, 22(3): 323-340.

[10] Mani, N., (2011). *Standardization of CMM Algorithms and Development of Inspection Maps for Geometric Tolerances*. Thesis of the Requirements for the Degree Master of Science Arizona state university, America.

[11] GB/T 1958-2004. (2002). Geometrical Product Specification (GPS)-General Concept-Part 1: Model for Geometric Specification and Verification.

[12] Guihua, L.I., Huajun, Z. and Xiushui, M.A., (2013). Online Measurement on Flatness and its Uncertainty of Small Work-piece. *Indonesian Journal of Electrical Engineering and Computer Science*, 11(2): 1041-1046.

[13] Gosavi, A. and Cudney, E., (2012). Form errors in precision metrology: a survey of measurement techniques. *Quality Engineering*, 24(3): 369-380.

[14] Flack, D., (2001). Measurement good practice Guide No. 42: CMM verification. *National Physical Laboratory*. ISSN 1368-6550. (pp. 29-34)

[15] Henzold, G., (2006). *Geometrical dimensioning and tolerancing for design, manufacturing and inspection: a handbook for geometrical product specification using ISO and ASME standards*. Butterworth-Heinemann, Second edition. (pp. 236-237).

[16] Mou, W.P., (1998), September. Test conditions for machining centers, part 7: accuracy of a finished test piece. International Standard. International Organization for Standardization, Geneva, Switzerland.

[17] Yamane, T., (1973). *Sample size determination. Statistics: An Introductory Analysis*. 3rd ed . Harper & Row, New York (pp. 1088).

[18] Kim, W.S. and Raman, S., (2000). On the selection of flatness measurement points in coordinate measuring machine inspection. *International Journal of Machine Tools and Manufacture*, 40(3): 427-443.